

# Generative Modelling With Inverse Heat Dissipation

Severi Rissanen

Aalto University

severi.rissanen@aalto.fi

Markus Heinonen

Aalto University

markus.o.heinonen@aalto.fi

Arno Solin

Aalto University

arno.solin@aalto.fi

## Abstract

While diffusion models have shown great success in image generation, their noise-inverting generative process does not explicitly consider the structure of images, such as their inherent multi-scale nature. Inspired by diffusion models and the desirability of coarse-to-fine modelling, we propose a new model that generates images through iteratively inverting the heat equation, a PDE that locally erases fine-scale information when run over the 2D plane of the image. In our novel methodology, the solution of the forward heat equation is interpreted as a variational approximation in a directed graphical model. We demonstrate promising image quality and point out emergent qualitative properties not seen in diffusion models, such as disentanglement of overall colour and shape in images and aspects of neural network interpretability. Spectral analysis on natural images positions our model as a type of dual to diffusion models and reveals implicit inductive biases in them.

## 1 Introduction

Diffusion and score-based generative models have become highly successful in generative modelling tasks [71, 72, 24, 75, 55, 18]. They are defined by a forward process that adds noise to input images, gradually drowning out their original information content. Images are generated by reverting the forward process iteratively with multiple passes through a neural network. Another iterative generative method is pixel-by-pixel autoregressive modelling [78, 77, 66]. However, the generation processes in diffusion and autoregressive models do not explicitly take into account the inductive biases of natural images, such as their inherent multi-scale nature or, in the case of diffusion models, even the fact that neighbouring pixels are next to each other and thus correlated. Yet, in other successful generative modelling settings, such as in GANs [20] and VAEs [41, 62], taking the multiple scales of effective resolution explicitly into account has resulted in dramatic improvements [34, 37, 76, 8, 60]. It is not clear how best to incorporate the inductive scale biases of natural images into iterative generative models.

On the other hand, the concept of resolution itself in deep learning methods has not received widespread attention, and usually scaling is based on sub-sampling pyramids, where the number of pixels decreases by a constant factor at each coarsening step [17, 34]. In classical computer vision, another approach is the so-called Gaussian scale-space [31, 81, 2, 42], where lower-resolution versions of an image are obtained by running the heat equation, a partial differential equation (PDE, see Fig. 1) that describes the dissipation of heat, over the surface of the image. Similarly to subsampling, the effect of the heat equation is to average out, or blur, the image and remove fine detail, but the dimensionality is not

**Information melting forward process**  $\frac{\partial \mathbf{u}}{\partial t} = \Delta \mathbf{u}$

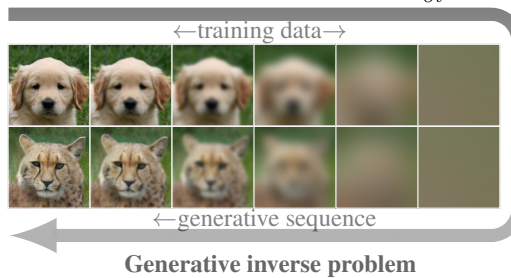


Figure 1: Example of the information destroying forward process (during training) and the generative inverse process (sampling).

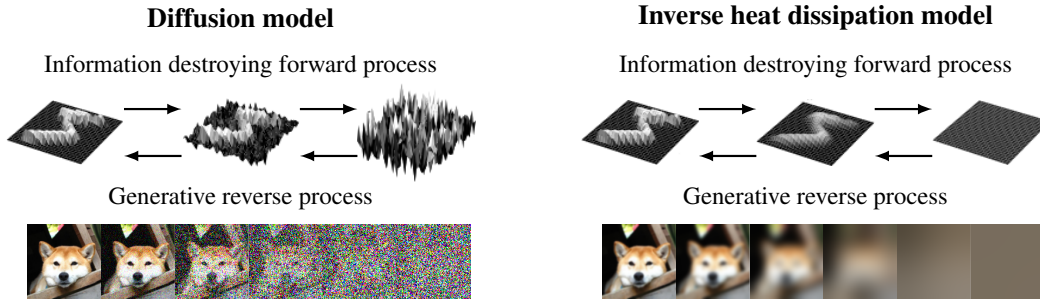


Figure 2: Comparison of generation by generative denoising and inverse heat diffusion, where the information destroying process affects the *pixel* space on the left and the *image* space on the right.

explicitly decreased and an arbitrary amount of different effective resolutions is allowed. The scale-space formalism has the theoretical advantage of being the only multi-scale representation of images that satisfies a set of *scale-space axioms*, such as rotational symmetry, invariance to shifts in the input image, and scale invariance [42, 2]. There are also links to how early biological vision represents signals [49, 50]. While the concept of scale-space has been utilized in the context of convolutional network architectures [82, 58], so far it has not been considered in generative models.

Motivated by the success of iterative generative models (in particular, diffusion models), multi-resolution in other models for image synthesis, and the theoretical desirability of the Gaussian scale-space, we propose a new type of generative model that combines these three. Similarly to diffusion models, we generate images by reversing an information-destroying forward process, but instead of adding noise to individual pixels, we deterministically reduce the effective resolution by running the heat equation over the image (*cf.* Fig. 2). That is, we perform diffusion *in the 2D image plane*. As most of the information of the original image has been erased, reverting the forward process stochastically results in the generation of new fine detail and generalization over the data set. The model accounts for the inductive bias of the pixel neighbourhood structure and the multi-scale nature of images, and allows an arbitrary number of computational steps and resolution levels. We call the new method the Inverse Heat Dissipation Model (IHDM).

The contributions of this paper are as follows. *(i)* We propose a novel generative model that iteratively reverses a sequence of images induced by the heat equation. It is based on interpreting the solution of the forward heat equation as a variational approximation in a directed graphical model. Similarly to diffusion models, it is simple to train with a static training objective, does not assume restrictions on neural network architectures and provides a lower bound on the marginal likelihood. *(ii)* Through taking into account the structure of natural images, the model results in properties not seen in diffusion models, such as interpretable aspects of neural network input gradients, disentanglement of overall colour and image shape and smooth interpolation capabilities. Our experimental results promising image quality on images up to  $256 \times 256$  pixel resolution. *(iii)* Through an analysis of the power spectral density of natural images, we show that diffusion models implicitly perform a different type of coarse-to-fine generation, shedding light on their inductive biases, as well as positioning our model as a type of dual to diffusion models. Visualizations are included in <https://aaltoml.github.io/generative-inverse-heat-dissipation/>

## 2 Related Work

Diffusion-type generative models, first introduced by Sohl-Dickstein et al. [69], have seen explosive development since the first papers on score-based generative modelling [71, 72], based on score-matching [29] and annealed Langevin dynamics. Score-based models were later shown to be closely connected with the original diffusion probabilistic model, based on maximizing a lower bound on the marginal likelihood in a directed graphical model [24]. Both formulations are often referred to as ‘diffusion models’ in the literature. A reverse SDE formalism that unified the framework was proposed by Song et al. [75] (later extended in [73, 28]), and further extensions in diffusion probabilistic models [55, 18] resulted in state-of-the-art performance on the ImageNet data set. Theoretical developments include the works in [15, 40]. Diffusion models have shown very promising performance in domains such as audio [5, 43, 6], text-to-image synthesis [59], categorical distributions [27], 3D

shape generation [4, 51, 85], video generation [26, 83], Riemannian manifolds [16], symbolic music generation [54], guided image synthesis [52] and text-to-image [59]. In contrast to these works, our main focus is not to improve empirical results on existing diffusion models, analyse their behaviour or extend them to new data domains. Instead, we take a step back from both diffusion models and autoregressive models and focus on the iterative generative sequence itself. Recent ideas introduced for diffusion models also include training diffusion models on different levels of resolution and cascading them together to improve the model performance [18, 64, 25]. The difference to us is that we consider the resolution-increasing as the basis of our model instead of a performance-boosting addition, and instead of using intermediate diffusion models, all computational steps increase the resolution.

Explicitly utilizing the hierarchy of resolutions in natural images has resulted in improved performance, *e.g.*, by training a stack of upsampling GAN layers that join to create a single image generator [17]. Other famous examples are the progressive GAN [34] and later the StyleGAN architectures [35–37, 68]. Resolution-based hierarchies in VAEs have brought them to rival GANs and other state-of-the-art models on different benchmarks [60, 76, 8]. Aside from these works, the architectures of other standard GANs and VAEs have been such that they start from low-resolution feature maps and increase the feature map resolution through upsampling layers.

Multiscale ideas in the context of autoregressive models have been proposed in the past, starting with the multi-scale pixelRNN model [78]. Possibly the closest one to our model is the work by Reed et al. [61], where the authors factorize the joint distribution as a subsampling pyramid such that generation starts from a pixelated image and progresses towards a high-resolution version. This resulted in faster sampling and the possibility to scale autoregressive modelling to high resolutions. Menick and Kalchbrenner [53] suggest a similar method based on resolution and bit-depth upscaling, although in a non-parallel way. Previously, generative models, including diffusion models, have been utilized for image deblurring [45, 46, 1, 80], super-resolution [48, 65, 14, 57, 7, 64, 12], and other types of inverse problems [38, 11, 32, 74, 10, 39]. While our model does effectively perform deblurring/super-resolution, the main difference to these works is that instead of using a pre-existing generative model to solve the inverse problem, we do the exact opposite and create a new generative model through iteratively solving an inverse problem using a loss function that directly reverses the heat equation.

### 3 Methods

We establish the methodology on an information destroying forward PDE process (Sec. 3.1), solve for time evolution, and formalize the generative reverse model (Sec. 3.2). We also show a connection to diffusion models through a spectral analysis of natural images (Sec. 3.3).

#### 3.1 Forward PDE Process

The main principle shared between our model and diffusion models is that the forward process erases information in the original image, so that reversing it, new information must be generated. In diffusion models, this is satisfied by adding noise; in our model, information is destroyed with deterministic averaging. We do this by running the heat equation, a linear partial differential equation (PDE) that describes the dissipation of heat, over the 2D plane of the image:

$$\frac{\partial}{\partial t} u(x, y, t) = \Delta u(x, y, t), \quad (1)$$

where  $u : \mathbb{R}^2 \times \mathbb{R}_+ \rightarrow \mathbb{R}$  is the idealized, continuous 2D plane of one channel of the image, and  $\Delta = \nabla^2$  is the Laplace operator. We use Neumann boundary conditions ( $\partial u / \partial x = \partial u / \partial y = 0$ ) with zero-derivatives at boundaries of the image bounding box. This means that as  $t \rightarrow \infty$ , the image will be entirely averaged out to the mean of the original pixel values in the image. While in principle, the heat equation could be reversible with infinite numerical precision, this is not the case in practice with any finite numerical accuracy due to the fundamental ill-posed nature of the inverse heat equation [33]. Thus, information is destroyed. The heat equation has an interpretation on macroscopic scale [67] in modelling the distribution of an ensemble of particles that are diffused in the 2D plane with Brownian motion. Entropy provides a connection to diffusion models: As the distribution of sharp images is effectively lower-dimensional than the entire  $N$ -dimensional pixel space, the entropy of the distribution in the diffusion forward process increases until noise fills the  $N$ -dimensional space. With the heat equation, entropy decreases until the distribution becomes essentially one-dimensional (3-dimensional in the case of RGB images).

The PDE model in Eq. (1) can be formally written in evolution equation form as  $u(x, y, t) = \mathcal{F}(t) u(x, y, t)|_{t=t_0}$ , where  $\mathcal{F}(t) = \exp[(t - t_0) \Delta]$  is an evolution operator given in terms of the operator exponential function (see, e.g., [13]). Even if the ideal evolution equation cannot be implemented in practice, we can use the formulation for efficiently solving the evolution equation in the function space *without explicit spatial discretization*, using the eigenbasis of the Laplace operator. Since we use the Neumann boundary conditions, the eigenbasis is a cosine basis (see full details in App. A.1). The observed finite-resolution image lies on a grid and the spectrum has a natural cut-off frequency (Nyquist limit), which means that we can formally write the operator in terms of a (finite) eigendecomposition  $\Delta \triangleq \mathbf{V} \mathbf{\Lambda} \mathbf{V}^\top$ , where  $\mathbf{V}^\top$  is the cosine basis projection matrix and  $\mathbf{\Lambda}$  is a diagonal matrix with negative squared frequencies on the diagonal. The initial state is then projected on to the basis with the discrete cosine transform ( $\tilde{\mathbf{u}} = \mathbf{V}^\top \mathbf{u} = \text{DCT}(\mathbf{u})$ ) in  $\mathcal{O}(N \log N)$  time. The solution is thus described by the finite-dimensional evolution model (in image  $\Leftrightarrow$  Fourier space):

$$\mathbf{u}(t) = \mathbf{F}(t) \mathbf{u}(0) = \exp(\mathbf{V} \mathbf{\Lambda} \mathbf{V}^\top t) \mathbf{u}(0) = \mathbf{V} \exp(\mathbf{\Lambda} t) \mathbf{V}^\top \mathbf{u}(0) \Leftrightarrow \tilde{\mathbf{u}}(t) = \exp(\mathbf{\Lambda} t) \tilde{\mathbf{u}}(0), \quad (2)$$

where  $\mathbf{F}(t) \in \mathbb{R}^{N \times N}$  (not expanded in practice) is the transition model and  $\mathbf{u}(0)$  the initial state. As  $\mathbf{\Lambda}$  is diagonal, the solution is fast to evaluate and implementable with a few lines of code, see App. A.1.

Another way to view the heat equation is through a well-known correspondence to the idea of Gaussian blur in image processing: In an infinite plane, simulating the heat equation up to time  $t$  equivalent to a convolution with a Gaussian kernel with variance  $\sigma_B^2 = 2t$  [3]. In fact, similarly to the method outlined above, one way to efficiently evaluate Gaussian blur is to use the discrete Fourier transform [19], and some form of Gaussian blur could be used to frame a very similar forward process to ours. It is useful to know that these two are essentially dual views to the same problem, and  $\sigma_B^2 = 2t$  can also be used as an effective length scale parameter for our process. The heat equation has the advantage that it exposes more directly the theoretical properties of the process, such as the scale-space, and is potentially better generalizable to other forward processes and data domains.

### 3.2 Generative Model Formulation

Next, we formulate a probabilistic forward-reverse model, which follows the general graphical model framework for diffusion models [69, 24], but using a subtly different inference process structure that is suited for the heat equation forward process. The generative process is a Markov chain of latent variables with  $\mathbf{u}_k$  that starts from a prior state  $\mathbf{u}_K$  and ends at the the observed variable  $\mathbf{u}_0$  as shown in Fig. 3a. Each latent has the same dimensionality as the data. Informally, we call this Markov chain the *reverse* process because the final training objective will cause it to reverse the heat equation with time steps  $t_K, t_{K-1}, \dots, t_0$ :

$$\begin{array}{l} \text{Reverse process /} \\ \text{Generative model} \end{array} \quad p_\theta(\mathbf{u}_{0:K}) = p(\mathbf{u}_K) \prod_{k=1}^K p_\theta(\mathbf{u}_{k-1} | \mathbf{u}_k), \quad (3)$$

where  $\theta$  are model parameters. Our goal is to maximize marginal likelihood of the data  $p(\mathbf{u}_0) = \int p_\theta(\mathbf{u}_0 | \mathbf{u}_{1:K}) p_\theta(\mathbf{u}_{1:K}) d\mathbf{u}_{1:K}$ . We derive a bound using the heat equation forward process, which formally corresponds to a variational posterior approximation in the latent variable model:

$$\begin{array}{l} \text{Forward process /} \\ \text{Inference distribution} \end{array} \quad q(\mathbf{u}_{1:K} | \mathbf{u}_0) = \prod_{k=1}^K q(\mathbf{u}_k | \mathbf{u}_0) = \prod_{k=1}^K \mathcal{N}(\mathbf{u}_k | \mathbf{F}(t_k) \mathbf{u}_0, \sigma^2 \mathbf{I}), \quad (4)$$

where  $\mathbf{F}(t_k)$  is the linear transformation corresponding to simulating the heat equation until time  $t_k$  and the standard deviation  $\sigma$  is a small constant (0.01 in our experiments, data scaled to  $[0, 1]$ ). The entire graphical model is shown in Fig. 3, where we highlight two points: (i) The forward process is not entirely deterministic with a non-zero  $\sigma$ . One can consider  $\sigma$  as an error-tolerance parameter that defines how close two paths along the deterministic heat equation have to be before they join together (see Fig. 3b). The problem from the point of view of the probabilistic model is that in principle, the heat equation is reversible, but we actually want the generation to branch in different directions that approximately correspond to sharper versions of the image. Intuitively, the conditional probabilities  $p_\theta(\mathbf{u}_{k-1} | \mathbf{u}_k)$  reverse the sequence of distributions induced by the forward process, and with a non-zero sigma, an initial state  $\mathbf{u}_K$  formally has a non-zero probability of going along different paths. The stochasticity during sampling then determines the trajectory, as illustrated in Fig. 3b. (ii) In diffusion probabilistic models, the inference distribution is defined as a Markov chain, as shown

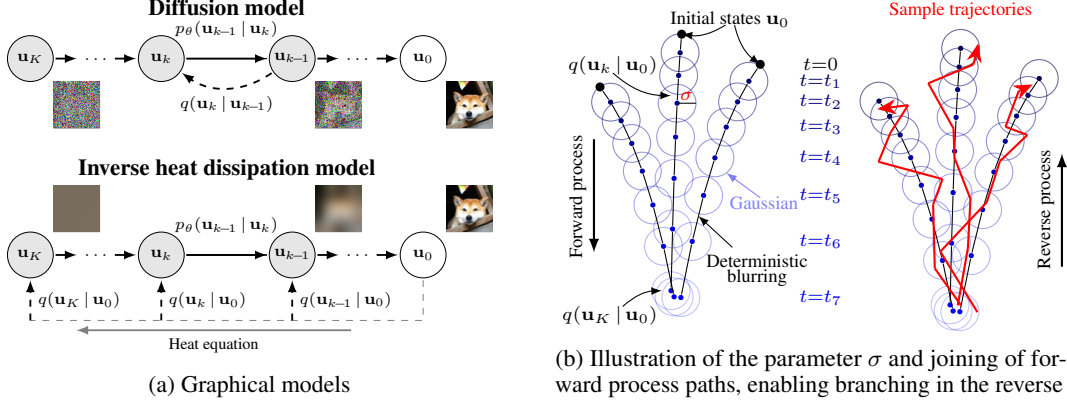


Figure 3: Graphical model of our vs. the diffusion model, and a sketch of how the stochasticity of  $q(\mathbf{u}_k | \mathbf{u}_0)$ , controlled by  $\sigma$ , allows the forward process paths to effectively merge in the probabilistic model. This makes branching to different alternative directions well-defined in the generative process.

in Fig. 3a. Here instead, the neighbouring latents are deterministically connected in the inference distribution through the heat equation, and the stochasticity is factorized.

Taking the VAE-type evidence lower bound for the marginal likelihood with the generative and inference distributions defined, we get

$$-\log p_\theta(\mathbf{u}_0) \leq \mathbb{E}_q \left[ -\log \frac{p_\theta(\mathbf{u}_{0:K})}{q(\mathbf{u}_{1:K} | \mathbf{u}_0)} \right] \quad (5)$$

$$= \mathbb{E}_q \left[ -\log \frac{p_\theta(\mathbf{u}_K)}{q(\mathbf{u}_K | \mathbf{u}_0)} - \sum_{k=2}^K \log \frac{p_\theta(\mathbf{u}_{k-1} | \mathbf{u}_k)}{q(\mathbf{u}_{k-1} | \mathbf{u}_0)} - \log p_\theta(\mathbf{u}_0 | \mathbf{u}_1) \right] \quad (6)$$

$$= \mathbb{E}_q \left[ \underbrace{\text{D}_{\text{KL}}[q(\mathbf{u}_K | \mathbf{u}_0) \| p(\mathbf{u}_K)]}_{L_K} + \sum_{k=2}^K \underbrace{\text{D}_{\text{KL}}[q(\mathbf{u}_{k-1} | \mathbf{u}_0) \| p_\theta(\mathbf{u}_{k-1} | \mathbf{u}_k)]}_{L_{k-1}} - \log p_\theta(\mathbf{u}_0 | \mathbf{u}_1) \right], \quad (7)$$

where the different parts of the process factorize in a similar, although somewhat simpler, way as in diffusion probabilistic models [69, 24]. Our choice for  $p_\theta(\mathbf{u}_{k-1} | \mathbf{u}_k)$  is

$$p_\theta(\mathbf{u}_{k-1} | \mathbf{u}_k) = \mathcal{N}(\mathbf{u}_{k-1} | \mu_\theta(\mathbf{u}_k, k), \delta^2 \mathbf{I}), \quad (8)$$

for which we further parametrize  $\mu_\theta(\mathbf{u}_k, k)$  with a skip connection such that  $\mu_\theta(\mathbf{u}_k, k) = \mathbf{u}_k + f_\theta(\mathbf{u}_k, k)$ . This is motivated by that we are trying to take a small step backwards in a differential equation, as noted in Eq. (13), and seems to stabilize training. The sampling noise standard deviation  $\delta$  is a free hyperparameter. The terms  $L_{k-1}$  are then KL divergences between Gaussian distributions

$$\mathbb{E}_q[L_{k-1}] = \mathbb{E}_q [\text{D}_{\text{KL}}[q(\mathbf{u}_{k-1} | \mathbf{u}_0) \| p_\theta(\mathbf{u}_{k-1} | \mathbf{u}_k)]] \quad (9)$$

$$= \frac{1}{2} \left( \frac{\sigma^2}{\delta^2} N - N + \frac{1}{\delta^2} \mathbb{E}_{q(\mathbf{u}_k | \mathbf{u}_0)} \left[ \left\| \underbrace{\mu_\theta(\mathbf{u}_k, k) - \mathbf{F}(t_{k-1}) \mathbf{u}_0}_{f_\theta(\mathbf{u}_k, k) - (\mathbf{F}(t_{k-1}) \mathbf{u}_0 - \mathbf{u}_k)} \right\|_2^2 \right] + 2N \log \frac{\delta}{\sigma} \right), \quad (10)$$

$$\mathbb{E}_q[L_0] = \mathbb{E}_q [-\log p_\theta(\mathbf{u}_0 | \mathbf{u}_1)] = \frac{1}{2\delta^2} \mathbb{E}_{q(\mathbf{u}_1 | \mathbf{u}_0)} \left[ \left\| \underbrace{\mu_\theta(\mathbf{u}_1, 1) - \mathbf{u}_0}_{f_\theta(\mathbf{u}_1, 1) - (\mathbf{u}_0 - \mathbf{u}_1)} \right\|_2^2 \right] + N \log(\delta\sqrt{2\pi}), \quad (11)$$

where  $N$  is the number of pixels in the image. Again, similarly to diffusion models, we evaluate the loss function with one Monte Carlo sample from the inference distribution  $q(\mathbf{u}_{1:K} | \mathbf{u}_0)$ . The losses on all levels are then direct MSE losses where we are trying to predict a slightly less blurred image from a blurred image that has a tiny bit of added noise with variance  $\sigma^2$ . When  $\mu_\theta(\mathbf{u}_k, k)$  is parameterized with the skip connection, the loss function resembles the denoising score matching objective, except that we are not predicting the denoised version of  $\mathbf{u}_k$ , but a less blurry  $\mathbf{u}_{k-1}$  instead. Sampling proceeds by alternating the mean update steps from the neural network and adding Gaussian noise with variance  $\delta$ . The training process is summarized in Alg. 1, and the sampling process in Alg. 2, both of which are simple to implement in practice.

**Algorithm 1** Loss function for a single data point

---


$$\begin{aligned} \mathbf{u}_0 &\sim \text{Sample from training data} \\ k &\sim \text{Sample from } \{1, \dots, K\} \\ \mathbf{u}_k &\leftarrow \mathbf{F}(t_k)\mathbf{u}_0 && \triangleright \text{ see Eq. (2)} \\ \mathbf{u}_{k-1} &\leftarrow \mathbf{F}(t_{k-1})\mathbf{u}_0 && \triangleright \text{ see Eq. (2)} \\ \varepsilon &\sim \mathcal{N}(\mathbf{0}, \sigma^2 \mathbf{I}) && \triangleright \text{ Training noise} \\ \hat{\mathbf{u}}_k &\leftarrow \mathbf{u}_k + \varepsilon && \triangleright \text{ Perturb image} \\ \text{Loss} &\leftarrow \|\mu_\theta(\hat{\mathbf{u}}_k, k) - \mathbf{u}_{k-1}\|_2^2 \end{aligned}$$


---

**Algorithm 2** Sampling

---


$$\begin{aligned} k &\leftarrow K && \triangleright \text{ Start from terminal state} \\ \mathbf{u} &\sim p(\mathbf{u}_K) && \triangleright \text{ Sample from the blurry prior} \\ \text{while } k > 0 &\text{ do} \\ \varepsilon_k &\sim \mathcal{N}(\mathbf{0}, \delta^2 \mathbf{I}) && \triangleright \text{ Sampling noise} \\ \mathbf{u} &\leftarrow \mu_\theta(\mathbf{u}, k) + \varepsilon_k && \triangleright \text{ Reverse step + noise} \\ k &\leftarrow k - 1 \\ \text{end while} \end{aligned}$$


---

For the prior distribution  $p(\mathbf{u}_K)$ , we can in principle use any standard density estimation technique, since the blurred images are effectively very low dimensional. We use a Gaussian kernel density estimate with variance  $\delta^2$ . If the blurred images at level  $K$  are low-dimensional and close enough to each other, this is a good estimate. Samples are obtained by taking a training example, blurring it with  $\mathbf{F}(t_K)$ , and adding noise with variance  $\delta^2$ . Using a kernel density estimate means that the term  $L_K$  is constant, but also tricky to calculate efficiently for log-likelihood evaluation due to the high-dimensional integral and multiple components in the kernel density estimate. In App. A.3, we provide a further variational upper bound on  $L_K$  that can be evaluated without numerical integration.

**3.3 Frequency-domain Analysis of the Generative Process**

The frequency behaviour of natural images provides a connection between the new model and diffusion models, and uncovers hidden inductive biases in diffusion models. The power spectral density of natural images obeys an approximate power law  $1/f^\alpha$ , where often  $\alpha \approx 2$  [79, 30]. When displayed on a log-log scale, the power spectral density is thus approximately a straight line. If we start the diffusion forward process and add a bit of noise, which has a flat power spectrum, the lowest frequencies of the image get drowned out by the noise while the higher frequencies stay intact. This continues until even the highest frequencies of the original image have disappeared. This is visualized in the red-coloured PSDs in Fig. 4. Thus, the spectrum of natural images implicitly induces to diffusion models the inductive bias that the reverse process must add increasing frequencies on top of the existing, lower frequencies: Generation starts from coarse structure and ends at the high-frequency details. While this is a rather straightforward observation to make once you note the  $1/f^\alpha$  frequency behaviour, we have not seen this stated in the literature so far, and could be interesting for designing better diffusion processes.

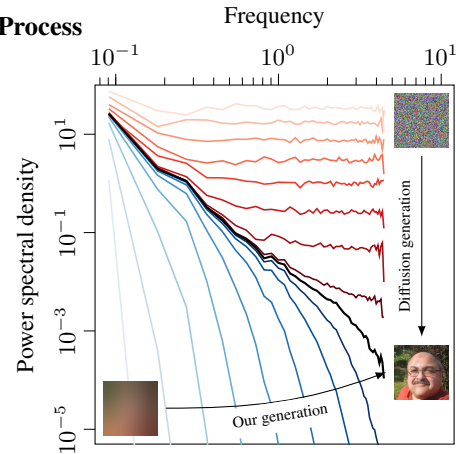


Figure 4: The  $1/f^\alpha$  power spectral density of natural images reveals that both models start the data generation from coarse, low-frequency structure and progress towards higher-frequency details. While diffusion models effectively layer frequencies one-by-one, our model increases the PSD of all frequencies jointly.

Analyzing further, we see a duality between our model and diffusion models: While the PSD of images in a diffusion model approach the  $1/f^\alpha$  line from above, our process approaches it from below, as visualized by the blue curves in Fig. 4. To see why this is the case, consider the explicit cosine series solution to the forward heat equation (alluded to in Sec. 3.1).

$$u(x, y, t) = \sum_n \sum_m A_{nm} e^{-\pi^2 (\frac{n^2}{W^2} + \frac{m^2}{H^2}) t} \cos\left(\frac{\pi n x}{W}\right) \cos\left(\frac{\pi m y}{H}\right). \quad (12)$$

Here  $A_{nm}$  are Fourier series coefficients with frequencies indexed by  $n$  and  $m$ , and  $W$  and  $H$  are the width and height of the image in pixels. The effect of the heat equation is to decay frequency components, with high frequencies decaying faster than low frequencies, explaining the shape of the PSD curves for our process in Fig. 4. Note that although there are similarities, a fundamental difference to diffusion models is that all frequencies are decayed at the same time instead of essentially removing them one-by-one. While both generative processes go from coarse to fine, in diffusion models the changes at each step are global instead of local, as frequency components span the entire image.



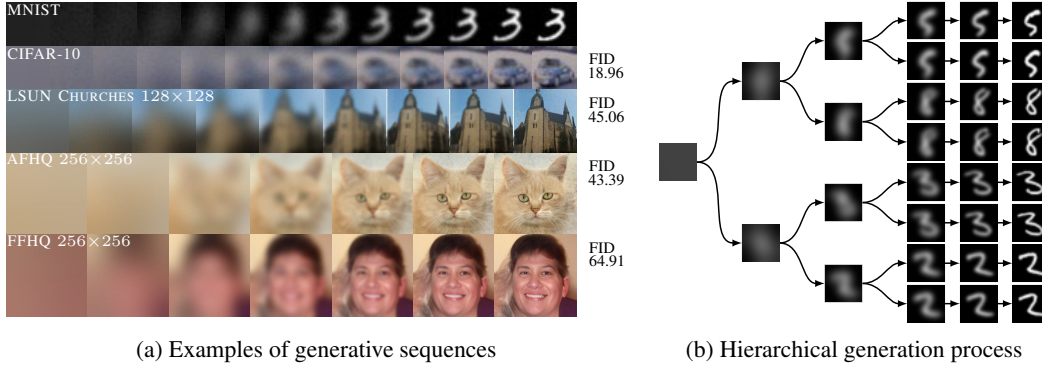


Figure 5: Generation sequences for different data sets. Generation starts from a flat image and adds progressively more detail. The process is stochastic, and any given image in the image can progress towards multiple directions as shown on the right. More uncurated generated samples in App. D.1.

## 4 Experiments

We present a range of experiments where we highlight capabilities of the proposed method, investigate hyperparameters, and analyse scale-space behaviour. In general, a main take-away is that the method in Algs. 1 and 2 works in practice, in spite of its apparent simplicity. We begin by showcasing generative sequences from the model on standard data sets, then analyse the effect of the two noise hyperparameters introduced, the training  $\sigma$  and sampling noise scale  $\delta$ . We then study the emergent property where the overall colour of the generated image is disentangled from its other features, and show that, contrary to standard diffusion models, our model can produce smooth interpolations between images. Finally, we show that the locality of the heat equation seems to have a direct effect on neural network behaviour, resulting in circularly symmetric, localized input gradients.

**Architecture and hyperparameters** In the experiments, similarly to many recent works on diffusion models [24, 75, 55, 18], we use a U-Net architecture [63] with residual blocks and self-attention layers in the low-resolution feature maps. We list the architectural details for different data sets in App. B. We use  $K = 200$  iteration steps on CIFAR-10 [44], AFHQ [9], and FFHQ [35], 100 steps on MNIST [47], and 400 on LSUN-CHURCHES [84]. The time  $t_k$  in the inference process is spaced logarithmically from near zero to  $t_K = \sigma_{B,\max}^2/2$  where  $\sigma_{B,\max}$  is the effective length-scale of blurring at the end of the process as described in Sec. 3.1. We set it to half the width of the image in all experiments, unless mentioned otherwise. For CIFAR-10, it is set to 24 pixel-widths.

**Generative sequences** Fig. 5a showcases the generative sequences from MNIST, CIFAR-10,  $128 \times 128$  LSUN-Churches,  $256 \times 256$  AFHQ, and  $256 \times 256$  FFHQ data sets. Generation starts from a blank image and progressively adds more fine-scale structure. Since the model is trained to revert the heat equation, the colour mass in the prior image is effectively redistributed to form a random image with the same average colour. The stochasticity of the process is visualized in Fig. 5b, where the sequence is split into two at specified time steps. Large-scale structure gets determined in the beginning and successive bifurcations lead into smaller and smaller changes in the output image. We present uncurated samples from all five data sets in App. D.1.

**Quantitative evaluation** We evaluate the FID scores on the chosen data sets, and list them on the right side of Fig. 5a. While the results are not yet as good as state-of-the-art diffusion models and GANs, we find the image quality promising. In the Supplemental Material, we also look at the marginal log-likelihood values and note that their optimal values don't correspond to optimal FID values when we vary the sampling noise parameter  $\delta$ .

**The effect of noise  $\sigma$**  As it is, the formulated loss function is almost as simple as it can be: The neural network is used simply to predict slightly less blurry images, using an MSE loss. The only complication was that we add noise with variance  $\sigma$  to the input image, and one could ask whether having no noise at all could work as well. In the Appendix we show that this is not the case, as the model generates essentially random images even with MNIST. Thus, having a non-zero  $\sigma$ , even a small one, seems to be necessary. In the experiments, we found that  $\sigma = 0.01$  seems to be a fairly robust value across data sets, and used that in all experiments.

**The effect of noise  $\delta$**  The sampling noise parameter  $\delta$  has also an important effect on the outcome, but the optimal value seems to be fairly robust across data sets, with a connection to the training noise parameter  $\sigma$ . In Fig. 6, we plot resulting images with different sampling noise parameters on CIFAR-10 and LSUN-Churches. With  $\delta = 0$ , the model mainly sharpens the prior image into some shape, and more detail is added as we increase it. Detail starts increasing particularly after  $\delta > 0.01 = \sigma$ , and after about  $\delta = 0.013$ , the images start to degenerate into noise. The optimal value is around  $\delta = 0.0125$  and  $\delta = 0.013$ , depending on the data set. Note that deterministic sampling is possible in diffusion models through the probability flow ODE [75] or the DDIM [70] formalisms, but here it seems that the noise is a key factor in producing the information content.

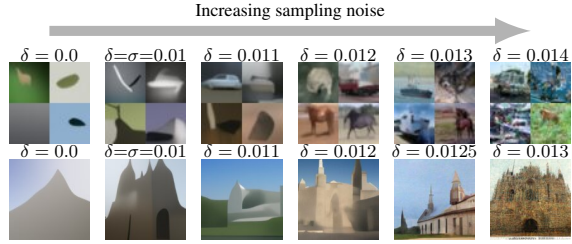


Figure 6: When the sampling noise parameter  $\delta=0$ , the model effectively sharpens the blurred image, with no new details added. As  $\delta$  increases over the training noise  $\sigma$ , the results become more fine-grained and detailed, and finally noisy.

**Disentangling colour and shape** If the endpoint of the forward process has been averaged well enough that the resulting images are the average colours of the original ones ( $\sigma_{B, \max} = \text{image size}$ ), the overall colour and other characteristics of the generated image become approximately disentangled. Fixing all the steps of noise added during the process and only changing the prior state  $\mathbf{u}_K$ , the sampling process tends to carve essentially the same image, just with different average colours, visualized in Fig. 7a for a  $128 \times 128$  FFHQ model. While other generative models with explicit modulation of resolution hierarchies have shown properties of disentanglement [35, 36, 22, 21], note that our method was not designed to exhibit this sort of behaviour, and instead seems to be an emergent feature.

**Smooth interpolation** We can also use this unique representation to interpolate between generated images, as shown in Fig. 7b. We use a linear interpolation on the input state  $\mathbf{u}_K$  and a spherical interpolation on the noise; more details in the Appendix. The same can be done with diffusion models as well, but as noted in [24], this results in non-smooth interpolations (Fig. 9 in the Appendix of [24]) We reproduce the result on FFHQ on a DDPM [24] model trained with 200 generation steps, to match with the number of steps in our FFHQ models. The lower panel of Fig. 7b shows that there are often jumps in the overall shape of the image, and the interpolation passes through features that are not present in either endpoint. This does not seem to happen with our model, which we believe is due to the hierarchical nature of the latent space.

**Inductive bias on the learned function** The fact that the forward process is mostly deterministic gives us information about the function that the neural network tries to approximate. While we use the DCT-based functional space approach in solving the forward process, a more elementary, but

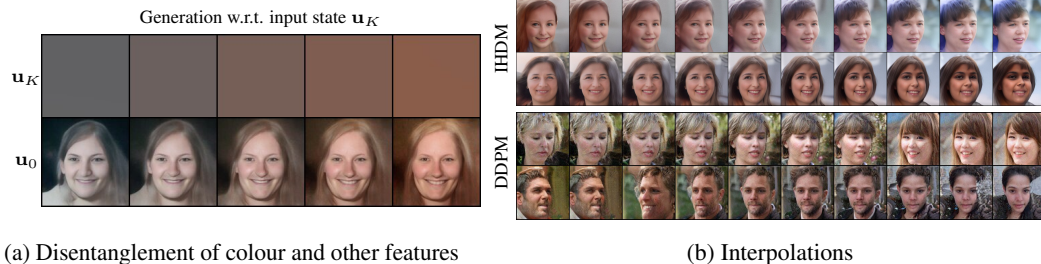


Figure 7: (a) By setting the noise added during the generative process to a constant value and changing the starting image which only contains information about the colour, highly similar faces with different overall color-schemes are created. (b) By also interpolating the noise steps in addition to the starting image, we obtain smooth interpolations between any two images in our model (IHDM). In a diffusion model (DDPM), the corresponding interpolation is non-smooth, passing through features that are not present in either endpoint, similarly to as noticed in [24]



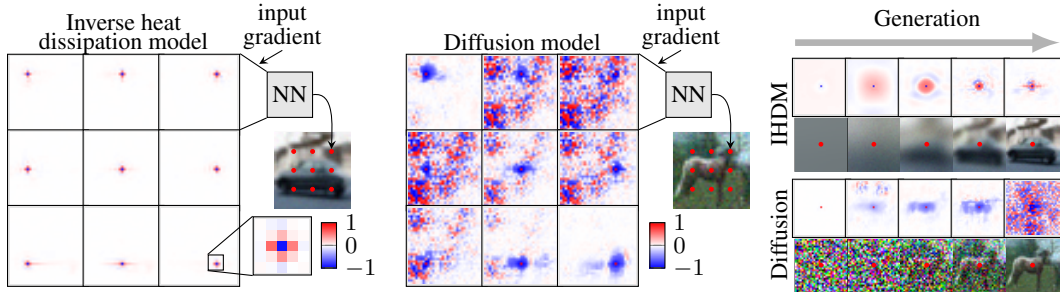


Figure 8: Left: The input gradients towards the end of the process for first channels of the pixels highlighted in the image for our model (IHDM). Middle: The same for a diffusion model (DDPM). Right: The input gradients for a pixel at the center of the image with respect to number of generation steps. The images correspond to the generation step in question. The colours are scaled to a symlog scale with a linear cut-off at 0.1 on the left and middle and 0.01 on the right.

instructive, option would have been a standard grid-based finite-difference approximation. It yields the following Euler step for the reverse heat equation:

$$u(x, y, t - dt) \approx u(x, y, t) - \begin{pmatrix} 0 & 1 & 0 \\ 1 & -4 & 1 \\ 0 & 1 & 0 \end{pmatrix} * u(x, y, t) dt. \quad (13)$$

Here,  $(x, y) \in \mathbb{I}^2$  are locations on the discrete pixel grid of the image, and ‘\*’ is a discrete convolution with the given sharpening kernel that corresponds to the negative Laplace operator. The intuition is that since small update steps along the ideal reverse heat equation are approximately convolutions, this should be reflected in the function learned by the neural network which largely consists of convolutional layers also. To probe into the network behaviour, we visualize the input gradients in Fig. 8 for our model and a diffusion model for comparison. The learned functions seem to be circularly symmetric and localized, in the sense that small perturbations at far-away pixels do not affect the output. In contrast, the dependence to input pixels is more global and complex for diffusion models.

## 5 Discussion and Conclusions

We have proposed a novel approach for generative modelling by stochastically inverting the heat equation. We find it intriguing that a generative model as simple as the one defined in Algs. 1 and 2 works in the first place, with good results without much need for hyperparameter tuning. We showed useful properties such as smooth interpolation and latent disentanglement, making the idea a promising direction for future research. The frequency analysis in Sec. 3.3 is interesting for diffusion model research in its own right, potentially opening new paths for designing diffusion processes and neural network architectures. While the obtained image quality is not yet on par with the state of the art, we view these results to be highly promising.

Potential future directions includes designing better neural network architectures, as the used version U-Net architecture has been adapted for diffusion models and is likely not optimal for our generative sequence. There are multiple directions to consider in the probabilistic model itself, such as generalizations beyond the standard Gaussian noise as introduced here, and the possibility of fully continuous-time formulation. Extensions of the heat dissipation forward process to other data domains, such as audio or graphs, would be possible. Finally, a wider point of our work is to broaden the view of iterative generative modelling: While our heat dissipation process is arguably natural for images and a complementary approach to diffusion models, other sequences could be considered as well, provided that the forward process erases information.

Our work is a part of the wider progress on generative modelling, and inherits much of the same potential for social impact. As the field progresses, increase in malicious uses of methods such as deepfakes are a worrying prospect. The proposed method could effectively be used for super-resolution tasks, and the way that the super-resolution is resolved will be affected by biases in the training data, which is something that users need to be aware of. On the other hand, generative models have been applied to inverse problems in medical imaging [32, 74, 10, 12], for instance. Another positive potential is to augment art and human creativity by including manual controls to the synthesis process, *e.g.*, text-conditional generation [59].

## References

- [1] M. Asim, F. Shamshad, and A. Ahmed. Blind image deconvolution using deep generative priors. *IEEE Transactions on Computational Imaging*, 6:1493–1506, 2020.
- [2] J. Babaud, A. P. Witkin, M. Baudin, and R. O. Duda. Uniqueness of the Gaussian kernel for scale-space filtering. *Transactions on Pattern Analysis and Machine Intelligence*, pages 26–33, 1986.
- [3] K. Bredies and D. Lorenz. *Mathematical Image Processing*. Springer, 2018.
- [4] R. Cai, G. Yang, H. Averbuch-Elor, Z. Hao, S. Belongie, N. Snavely, and B. Hariharan. Learning gradient fields for shape generation. In *Proceedings of the European Conference on Computer Vision (ECCV)*, pages 364–381. Springer, 2020.
- [5] N. Chen, Y. Zhang, H. Zen, R. J. Weiss, M. Norouzi, and W. Chan. Wavegrad: Estimating gradients for waveform generation. In *International Conference on Learning Representations (ICLR)*, 2021.
- [6] N. Chen, Y. Zhang, H. Zen, R. J. Weiss, M. Norouzi, N. Dehak, and W. Chan. WaveGrad 2: Iterative refinement for text-to-speech synthesis. In *Proceedings of Interspeech*, pages 3765–3769, 2021.
- [7] Y. Chen, Y. Tai, X. Liu, C. Shen, and J. Yang. Fsrnet: End-to-end learning face super-resolution with facial priors. In *Proceedings of the IEEE/CVF Conference on Computer Vision and Pattern Recognition (CVPR)*, pages 2492–2501, 2018.
- [8] R. Child. Very deep VAEs generalize autoregressive models and can outperform them on images. In *International Conference on Learning Representations (ICLR)*, 2021.
- [9] Y. Choi, Y. Uh, J. Yoo, and J.-W. Ha. StarGAN v2: Diverse image synthesis for multiple domains. In *Proceedings of the IEEE/CVF Conference on Computer Vision and Pattern Recognition (CVPR)*, pages 8188–8197, 2020.
- [10] H. Chung and J. C. Ye. Score-based diffusion models for accelerated MRI. *Medical Image Analysis*, page 102479, 2022.
- [11] H. Chung, B. Sim, and J. C. Ye. Come-closer-diffuse-faster: Accelerating conditional diffusion models for inverse problems through stochastic contraction. *arXiv preprint arXiv:2112.05146*, 2021.
- [12] H. Chung, E. S. Lee, and J. C. Ye. MR image denoising and super-resolution using regularized reverse diffusion. *arXiv preprint arXiv:2203.12621*, 2022.
- [13] G. Da Prato and J. Zabczyk. *Stochastic Equations in Infinite Dimensions*, volume 45 of *Encyclopedia of Mathematics and its Applications*. Cambridge University Press, 1992.
- [14] R. Dahl, M. Norouzi, and J. Shlens. Pixel recursive super resolution. In *Proceedings of the IEEE/CVF International Conference on Computer Vision (ICCV)*, pages 5439–5448, 2017.
- [15] V. De Bortoli, J. Thornton, J. Heng, and A. Doucet. Diffusion schrödinger bridge with applications to score-based generative modeling. In *Advances in Neural Information Processing Systems (NeurIPS)*, volume 34, pages 17695–17709. Curran Associates, Inc., 2021.
- [16] V. De Bortoli, E. Mathieu, M. Hutchinson, J. Thornton, Y. W. Teh, and A. Doucet. Riemannian score-based generative modeling. *arXiv preprint arXiv:2202.02763*, 2022.
- [17] E. L. Denton, S. Chintala, A. Szlam, and R. Fergus. Deep generative image models using a Laplacian pyramid of adversarial networks. In *Advances in Neural Information Processing Systems (NeurIPS)*, volume 28, pages 1486–1494. Curran Associates, Inc., 2015.
- [18] P. Dhariwal and A. Nichol. Diffusion models beat gans on image synthesis. In *Advances in Neural Information Processing Systems (NeurIPS)*, volume 34, pages 8780–8794. Curran Associates, Inc., 2021.
- [19] R. C. Gonzalez and R. E. Woods. *Digital Image Processing*. Pearson, 2018.
- [20] I. Goodfellow, J. Pouget-Abadie, M. Mirza, B. Xu, D. Warde-Farley, S. Ozair, A. Courville, and Y. Bengio. Generative adversarial nets. In *Advances in Neural Information Processing Systems (NIPS)*, volume 27, pages 2672–2680. Curran Associates, Inc., 2014.
- [21] E. Härkönen, A. Hertzmann, J. Lehtinen, and S. Paris. GANSpace: Discovering interpretable GAN controls. In *Advances in Neural Information Processing Systems (NeurIPS)*, volume 33, pages 9841–9850. Curran Associates, Inc., 2020.

- [22] A. Heljakka, Y. Hou, J. Kannala, and A. Solin. Deep automodulators. In *Advances in Neural Information Processing Systems (NeurIPS)*, volume 33, pages 13702–13713. Curran Associates, Inc., 2020.
- [23] J. R. Hershey and P. A. Olsen. Approximating the Kullback Leibler divergence between gaussian mixture models. In *2007 IEEE International Conference on Acoustics, Speech and Signal Processing (ICASSP)*, volume 4, pages IV–317. IEEE, 2007.
- [24] J. Ho, A. Jain, and P. Abbeel. Denoising diffusion probabilistic models. In *Advances in Neural Information Processing Systems (NeurIPS)*, volume 33, pages 6840–6851. Curran Associates, Inc., 2020.
- [25] J. Ho, C. Saharia, W. Chan, D. J. Fleet, M. Norouzi, and T. Salimans. Cascaded diffusion models for high fidelity image generation. *Journal of Machine Learning Research*, 23(47):1–33, 2022.
- [26] J. Ho, T. Salimans, A. Gritsenko, W. Chan, M. Norouzi, and D. J. Fleet. Video diffusion models. *arXiv preprint arXiv:2204.03458*, 2022.
- [27] E. Hoogeboom, D. Nielsen, P. Jaini, P. Forré, and M. Welling. Argmax flows and multinomial diffusion: Learning categorical distributions. In *Advances in Neural Information Processing Systems (NeurIPS)*, volume 34, pages 12454–12465. Curran Associates, Inc., 2021.
- [28] C.-W. Huang, J. H. Lim, and A. C. Courville. A variational perspective on diffusion-based generative models and score matching. In *Advances in Neural Information Processing Systems (NeurIPS)*, volume 34, pages 22863–22876. Curran Associates, Inc., 2021.
- [29] A. Hyvärinen and P. Dayan. Estimation of non-normalized statistical models by score matching. *Journal of Machine Learning Research*, 6(4), 2005.
- [30] A. Hyvärinen, J. Hurri, and P. O. Hoyer. *Natural Image Statistics: A Probabilistic Approach to Early Computational Vision*, volume 39. Springer Science & Business Media, 2009.
- [31] T. Iijima. Observation theory of two-dimensional visual patterns. *Technical Group on Automata and Automatic Control, IECE, Japan*, 1962.
- [32] A. Jalal, M. Arvinte, G. Daras, E. Price, A. G. Dimakis, and J. Tamir. Robust compressed sensing mri with deep generative priors. In *Advances in Neural Information Processing Systems (NeurIPS)*, volume 34, pages 14938–14954. Curran Associates, Inc., 2021.
- [33] J. Kaipio and E. Somersalo. *Statistical and Computational Inverse Problems*. Springer Science & Business Media, 2006.
- [34] T. Karras, T. Aila, S. Laine, and J. Lehtinen. Progressive growing of GANs for improved quality, stability, and variation. In *International Conference on Learning Representations (ICLR)*, 2018.
- [35] T. Karras, S. Laine, and T. Aila. A style-based generator architecture for generative adversarial networks. In *Proceedings of the IEEE/CVF Conference on Computer Vision and Pattern Recognition (CVPR)*, pages 4401–4410, 2019.
- [36] T. Karras, S. Laine, M. Aittala, J. Hellsten, J. Lehtinen, and T. Aila. Analyzing and improving the image quality of stylegan. In *Proceedings of the IEEE/CVF Conference on Computer Vision and Pattern Recognition (CVPR)*, pages 8110–8119, 2020.
- [37] T. Karras, M. Aittala, S. Laine, E. Härkönen, J. Hellsten, J. Lehtinen, and T. Aila. Alias-free generative adversarial networks. In *Advances in Neural Information Processing Systems (NeurIPS)*, volume 34, pages 852–863. Curran Associates, Inc., 2021.
- [38] B. Kavar, G. Vaksman, and M. Elad. Snips: Solving noisy inverse problems stochastically. In *Advances in Neural Information Processing Systems (NeurIPS)*, volume 34, pages 21757–21769. Curran Associates, Inc., 2021.
- [39] B. Kavar, M. Elad, S. Ermon, and J. Song. Denoising diffusion restoration models. *arXiv preprint arXiv:2201.11793*, 2022.
- [40] D. Kingma, T. Salimans, B. Poole, and J. Ho. Variational diffusion models. In *Advances in Neural Information Processing Systems (NeurIPS)*, volume 34, pages 21696–21707. Curran Associates, Inc., 2021.
- [41] D. P. Kingma and M. Welling. Auto-encoding variational Bayes. In *International Conference on Learning Representations (ICLR)*, 2014.
- [42] J. J. Koenderink. The structure of images. *Biological Cybernetics*, 50(5):363–370, 1984.

- [43] Z. Kong, W. Ping, J. Huang, K. Zhao, and B. Catanzaro. Diffwave: A versatile diffusion model for audio synthesis. In *International Conference on Learning Representations (ICLR)*, 2021.
- [44] A. Krizhevsky. *Learning Multiple Layers of Features from Tiny Images*. MSc thesis, University of Toronto, Canada, 2009.
- [45] O. Kupyn, V. Budzan, M. Mykhailych, D. Mishkin, and J. Matas. DeblurGAN: Blind motion deblurring using conditional adversarial networks. In *Proceedings of the IEEE/CVF Conference on Computer Vision and Pattern Recognition (CVPR)*, pages 8183–8192, 2018.
- [46] O. Kupyn, T. Martyniuk, J. Wu, and Z. Wang. DeblurGAN-v2: Deblurring (orders-of-magnitude) faster and better. In *Proceedings of the IEEE/CVF International Conference on Computer Vision (ICCV)*, pages 8878–8887, 2019.
- [47] Y. LeCun, L. Bottou, Y. Bengio, and P. Haffner. Gradient-based learning applied to document recognition. *Proceedings of the IEEE*, 86(11):2278–2324, 1998.
- [48] C. Ledig, L. Theis, F. Huszár, J. Caballero, A. Cunningham, A. Acosta, A. Aitken, A. Tejani, J. Totz, Z. Wang, et al. Photo-realistic single image super-resolution using a generative adversarial network. In *Proceedings of the IEEE/CVF Conference on Computer Vision and Pattern Recognition (CVPR)*, pages 4681–4690, 2017.
- [49] T. Lindeberg. A computational theory of visual receptive fields. *Biological Cybernetics*, 107(6):589–635, 2013.
- [50] T. Lindeberg. Invariance of visual operations at the level of receptive fields. *PLoS One*, 8(7):e66990, 2013.
- [51] S. Luo and W. Hu. Diffusion probabilistic models for 3d point cloud generation. In *Proceedings of the IEEE/CVF Conference on Computer Vision and Pattern Recognition (CVPR)*, pages 2837–2845, 2021.
- [52] C. Meng, Y. Song, J. Song, J. Wu, J.-Y. Zhu, and S. Ermon. SDEdit: Image synthesis and editing with stochastic differential equations. *arXiv preprint arXiv:2108.01073*, 2021.
- [53] J. Menick and N. Kalchbrenner. Generating high fidelity images with subscale pixel networks and multidimensional upscaling. In *International Conference on Learning Representations (ICLR)*, 2019.
- [54] G. Mittal, J. H. Engel, C. Hawthorne, and I. Simon. Symbolic music generation with diffusion models. In *Proceedings of the 22nd International Society for Music Information Retrieval Conference (ISMIR)*, pages 468–475, 2021.
- [55] A. Q. Nichol and P. Dhariwal. Improved denoising diffusion probabilistic models. In *Proceedings of the 38th International Conference on Machine Learning (ICML)*, volume 139 of *Proceedings of Machine Learning Research*, pages 8162–8171. PMLR, 2021.
- [56] G. Parmar, R. Zhang, and J.-Y. Zhu. On aliased resizing and surprising subtleties in gan evaluation. In *CVPR*, 2022.
- [57] N. Parmar, A. Vaswani, J. Uszkoreit, L. Kaiser, N. Shazeer, A. Ku, and D. Tran. Image transformer. In *Proceedings of the 35th International Conference on Machine Learning (ICML)*, volume 80 of *Proceedings of Machine Learning Research*, pages 4052–4061. PMLR, 2018.
- [58] S. L. Pinteá, N. Tömen, S. F. Goes, M. Loog, and J. C. van Gemert. Resolution learning in deep convolutional networks using scale-space theory. *Transactions on Image Processing*, 30:8342–8353, 2021.
- [59] A. Ramesh, P. Dhariwal, A. Nichol, C. Chu, and M. Chen. Hierarchical text-conditional image generation with clip latents. *arXiv preprint arXiv:2204.06125*, 2022.
- [60] A. Razavi, A. van den Oord, and O. Vinyals. Generating diverse high-fidelity images with VQ-VAE-2. In *Advances in Neural Information Processing Systems (NeurIPS)*, volume 32, pages 14866–14876. Curran Associates, Inc., 2019.
- [61] S. E. Reed, A. van den Oord, N. Kalchbrenner, S. G. Colmenarejo, Z. Wang, Y. Chen, D. Belov, and N. de Freitas. Parallel multiscale autoregressive density estimation. In *Proceedings of the 34th International Conference on Machine Learning (ICML)*, volume 70 of *Proceedings of Machine Learning Research*, pages 2912–2921. PMLR, 2017.
- [62] D. J. Rezende, S. Mohamed, and D. Wierstra. Stochastic backpropagation and approximate inference in deep generative models. In *Proceedings of the 31th International Conference on Machine Learning (ICML)*, volume 32 of *Proceedings in Machine Learning Research*, pages 1278–1286. PMLR, 2014.

- [63] O. Ronneberger, P. Fischer, and T. Brox. U-net: Convolutional networks for biomedical image segmentation. In *International Conference on Medical Image Computing and Computer-assisted Intervention*, pages 234–241. Springer, 2015.
- [64] C. Saharia, J. Ho, W. Chan, T. Salimans, D. J. Fleet, and M. Norouzi. Image super-resolution via iterative refinement. *arXiv:2104.07636*, 2021.
- [65] M. S. Sajjadi, B. Scholkopf, and M. Hirsch. Enhancenet: Single image super-resolution through automated texture synthesis. In *Proceedings of the IEEE/CVF International Conference on Computer Vision (ICCV)*, pages 4491–4500, 2017.
- [66] T. Salimans, A. Karpathy, X. Chen, and D. P. Kingma. PixelCNN++: Improving the PixelCNN with discretized logistic mixture likelihood and other modifications. In *International Conference on Learning Representations (ICLR)*, 2017.
- [67] S. Särkkä and A. Solin. *Applied Stochastic Differential Equations*. Cambridge University Press, Cambridge, UK, 2019.
- [68] A. Sauer, K. Schwarz, and A. Geiger. StyleGAN-XL: Scaling StyleGAN to large diverse datasets. *arXiv preprint arXiv:2202.00273*, 2022.
- [69] J. Sohl-Dickstein, E. A. Weiss, N. Maheswaranathan, and S. Ganguli. Deep unsupervised learning using nonequilibrium thermodynamics. In *Proceedings of the 32nd International Conference on Machine Learning (ICML)*, volume 37 of *Proceedings of Machine Learning Research*, pages 2256–2265. PMLR, 2015.
- [70] J. Song, C. Meng, and S. Ermon. Denoising diffusion implicit models. In *International Conference on Learning Representations (ICLR)*, 2021.
- [71] Y. Song and S. Ermon. Generative modeling by estimating gradients of the data distribution. In *Advances in Neural Information Processing Systems (NeurIPS)*, volume 32, pages 11918–11930. Curran Associates, Inc., 2019.
- [72] Y. Song and S. Ermon. Improved techniques for training score-based generative models. In *Advances in Neural Information Processing Systems (NeurIPS)*, volume 33, pages 12438–12448. Curran Associates, Inc., 2020.
- [73] Y. Song, C. Durkan, I. Murray, and S. Ermon. Maximum likelihood training of score-based diffusion models. In *Advances in Neural Information Processing Systems (NeurIPS)*, volume 34, pages 1415–1428. Curran Associates, Inc., 2021.
- [74] Y. Song, L. Shen, L. Xing, and S. Ermon. Solving inverse problems in medical imaging with score-based generative models. *arXiv preprint arXiv:2111.08005*, 2021.
- [75] Y. Song, J. Sohl-Dickstein, D. P. Kingma, A. Kumar, S. Ermon, and B. Poole. Score-based generative modeling through stochastic differential equations. In *International Conference on Learning Representations (ICLR)*, 2021.
- [76] A. Vahdat and J. Kautz. NVAE: A deep hierarchical variational autoencoder. In *Advances in Neural Information Processing Systems (NeurIPS)*, volume 33, pages 19667–19679. Curran Associates, Inc., 2020.
- [77] A. van den Oord, N. Kalchbrenner, L. Espeholt, K. Kavukcuoglu, O. Vinyals, and A. Graves. Conditional image generation with PixelCNN decoders. In *Advances in Neural Information Processing Systems (NeurIPS)*, volume 29. Curran Associates, Inc., 2016.
- [78] A. van den Oord, N. Kalchbrenner, and K. Kavukcuoglu. Pixel recurrent neural networks. In *Proceedings of the 33rd International Conference on Machine Learning (ICML)*, volume 48 of *Proceedings of Machine Learning Research*, pages 1747–1756. PMLR, 2016.
- [79] A. van der Schaaf and J. van Hateren. Modelling the power spectra of natural images: Statistics and information. *Vision Research*, 36(17):2759–2770, 1996.
- [80] J. Whang, M. Delbracio, H. Talebi, C. Saharia, A. G. Dimakis, and P. Milanfar. Deblurring via stochastic refinement. *arXiv preprint arXiv:2112.02475*, 2021.
- [81] A. P. Witkin. Scale-space filtering. In *Readings in Computer Vision*, pages 329–332. Elsevier, 1987.
- [82] D. Worrall and M. Welling. Deep scale-spaces: Equivariance over scale. In *Advances in Neural Information Processing Systems (NeurIPS)*, volume 32, pages 7366–7378. Curran Associates, Inc., 2019.



- [83] R. Yang, P. Srivastava, and S. Mandt. Diffusion probabilistic modeling for video generation. *arXiv preprint arXiv:2203.09481*, 2022.
- [84] F. Yu, A. Seff, Y. Zhang, S. Song, T. Funkhouser, and J. Xiao. LSUN: Construction of a large-scale image dataset using deep learning with humans in the loop. *arXiv preprint arXiv:1506.03365*, 2015.
- [85] L. Zhou, Y. Du, and J. Wu. 3d shape generation and completion through point-voxel diffusion. In *Proceedings of the IEEE/CVF International Conference on Computer Vision (ICCV)*, pages 5826–5835, 2021.

---

# Supplementary Material: Generative Modelling With Inverse Heat Dissipation

---

## A Derivation of Method Details

### A.1 Numerical Solution of the Heat Equation with Neumann Boundary Conditions Using the Discrete Cosine Transform

We expand the presentation of the approach taken in Sec. 3.1 and provide some further details on the derivation that highlights various appealing aspects of our approach. The material here is not novel, but is included for completeness.

We use the partial differential (PDE) model

$$\frac{\partial}{\partial t} u(x, y, t) = \Delta u(x, y, t), \quad (14)$$

where  $u : \mathbb{R}^2 \times \mathbb{R}_+ \rightarrow \mathbb{R}$  is the idealized, continuous 2D plane of one channel of the image, and  $\Delta = \nabla^2$  is the Laplace operator. Rather than discretizing the operator by a finite-difference scheme (see Eq. (13) for discussion in the main paper), we take an alternative approach where we solve the heat equation in the function space by projecting the problem onto the eigenbasis of the operator. The benefits are good numerical accuracy and scalability to large images. The workflow is as follows: (i) Rewrite the PDE as an evolution equation. (ii) Choose boundary conditions (Neumann, *i.e.* the image ‘averages out’ as  $t \rightarrow \infty$ ). (iii) Solve the associated eigenvalue problem (eigenbasis of the operator) which in this case results in a cosine basis. (iv) The image is on a regular grid, so we can use the Discrete Cosine Transform (DCT) for projection. This also means that there is a cut-off frequency for the problem that makes it finite-dimensional.

**Evolution equation** Following the steps written out above, the PDE model in Eq. (14) can be formally written in evolution equation form as

$$u(x, y, t) = \mathcal{F}(t) u(x, y, t_0), \quad (15)$$

where  $\mathcal{F}(t) = \exp[(t - t_0) \Delta]$  is an evolution operator given in terms of the operator exponential function (see, *e.g.*, [13]). It is worth noting that instead of the Laplacian we could also consider more general (pseudo-)differential operators to describe more complicated dissipation processes.

**Choice of boundary conditions** We choose to Neumann boundary conditions ( $\partial u / \partial x = \partial u / \partial y = 0$ ) with zero-derivatives at boundaries of the image bounding box. This means that as  $t \rightarrow \infty$ , the image will be entirely averaged out to the mean of the original pixel values in the image. We could choose some other boundary conditions as well, in many cases without loss of generality. Formally:

$$\left. \begin{aligned} \frac{\partial}{\partial x} u(0, y, t) &= 0 & \frac{\partial}{\partial x} u(W, y, t) &= 0 \\ \frac{\partial}{\partial y} u(x, 0, t) &= 0 & \frac{\partial}{\partial y} u(x, H, t) &= 0 \end{aligned} \right\} \text{Boundary conditions} \quad (16)$$

$$u(x, y, t_0) = f(x, y) \quad \text{Initial condition,} \quad (17)$$

where  $W$  is the width of the image and  $H$  is the height.

**Solve associated eigenvalue problem** For the (negative) Laplace operator, which is positive definite and Hermitian, the solutions to the eigenvalue problem

$$-\Delta \phi_j(x, y) = \lambda_j \phi_j(x, y), \quad \text{for } (x, y) \in \Omega, \quad (18)$$

$$\frac{\partial \phi_j(x, y)}{\partial x} = \frac{\partial \phi_j(x, y)}{\partial y} = 0, \quad \text{for } (x, y) \in \partial\Omega, \quad (19)$$

yields orthonormal eigenfunctions  $\phi_j(\cdot)$  with respect to the associated inner product, meaning that the corresponding operator is diagonalizable. If  $\Omega$  is a rectangular domain and we consider the problem in Cartesian coordinates, the eigenbasis (solution to the eigenvalue problem above under the boundary conditions) turns out to be a (separable) cosine basis:

$$\phi_{n,m}(x, y) \sim \cos\left(\frac{\pi n x}{W}\right) \cos\left(\frac{\pi m y}{H}\right) \quad (20)$$

$$\lambda_{n,m} = \pi^2 \left( \frac{n^2}{W^2} + \frac{m^2}{H^2} \right). \quad (21)$$

Writing out the result of the evolution operator  $\mathcal{F}(t) = \exp[(t - t_0) \Delta]$  explicitly,

$$u(x, y, t) = \sum_{n=0}^{\infty} \sum_{m=0}^{\infty} A_{nm} e^{-\pi^2 \left( \frac{n^2}{W^2} + \frac{m^2}{H^2} \right) (t-t_0)} \cos\left(\frac{\pi n x}{W}\right) \cos\left(\frac{\pi m y}{H}\right), \quad (22)$$

which is a Fourier series where  $A_{n,m}$  are the coefficients from projecting the initial state  $u(x, y, t_0)$  to the eigenfunctions  $\phi_{n,m}(x, y)$ .

**Leverage the regularity of the image** If we consider the pixels in the image to be samples from the underlying continuous surface  $u(x, y)$  that lie on a regular grid, the projection onto this basis can be done with the discrete cosine transform ( $\tilde{\mathbf{u}} = \mathbf{V}^\top \mathbf{u} = \text{DCT}(\mathbf{u})$ ). As the observed finite-resolution image has a natural cut-off frequency (Nyquist limit due to ‘distance’ between pixel centers), the projection onto and from the cosine basis can be done with perfect accuracy due to the Nyquist-Shannon sampling theorem. Formally, a finite-dimensional Laplace operator can be written out as the eigendecomposition  $\Delta \triangleq \mathbf{V} \Lambda \mathbf{V}^\top$ , where  $\Lambda$  is a diagonal matrix containing the negative squared frequencies  $-\pi^2 \left( \frac{n^2}{W^2} + \frac{m^2}{H^2} \right)$  and  $\mathbf{V}^\top$  is the discrete cosine transform projection matrix. The evolution equation, and our numerical solution to the heat equation, can thus be described by the finite-dimensional evolution model (in image  $\Leftrightarrow$  Fourier space):

$$\mathbf{u}(t) = \mathbf{F}(t) \mathbf{u}(0) = \exp(\mathbf{V} \Lambda \mathbf{V}^\top t) \mathbf{u}(0) = \mathbf{V} \exp(\Lambda t) \mathbf{V}^\top \mathbf{u}(0) \Leftrightarrow \tilde{\mathbf{u}}(t) = \exp(\Lambda t) \tilde{\mathbf{u}}(0), \quad (23)$$

where  $\mathbf{F}(t) \in \mathbb{R}^{N \times N}$  is the transition model and  $\mathbf{u}(0)$  the initial state.  $\mathbf{F}(t)$  is not expanded out in practice, but instead we use the DCT and inverse DCT, which are  $O(N \log N)$  operations. As  $\Lambda$  is diagonal, the Fourier-space model is fast to evaluate. The algorithm in practice is summarized as a Python snippet in Alg. 3.

---

**Algorithm 3** Python code for calculating the forward process

---

```

1 import numpy as np
2 from scipy.fftpack import dct, idct
3 def heat_eq_forward(u, t):
4     # Assuming the image u is an (KxK) numpy array
5     freqs = np.pi*np.linspace(0,K-1,K)/K
6     frequencies_squared = freqs[:,None]**2 + freqs[None,:]**2
7     u_proj = dct(u, axis=0, norm='ortho')
8     u_proj = dct(u_proj, axis=1, norm='ortho')
9     u_proj = np.exp(- frequencies_squared * t) * u_proj
10    u_reconstructed = idct(u_proj, axis=0, norm='ortho')
11    u_reconstructed = idct(u_reconstructed, axis=1, norm='ortho')
12    return u_reconstructed

```

---

## A.2 Derivation of the Variational Lower Bound

This section contains a derivation for the variational bound in more detail than what was presented in the main text. Recall the definitions for the generative Markov chain and the inference distribution:

$$\begin{array}{l} \text{Reverse process /} \\ \text{Generative model} \end{array} \quad p_\theta(\mathbf{u}_{0:K}) = p(\mathbf{u}_K) \prod_{k=1}^K p_\theta(\mathbf{u}_{k-1} | \mathbf{u}_k) = p(\mathbf{u}_K) \prod_{k=1}^K \mathcal{N}(\mathbf{u}_{k-1} | \mu_\theta(\mathbf{u}_k, k), \delta^2 \mathbf{I})$$

$$\begin{array}{l} \text{Forward process /} \\ \text{Inference distribution} \end{array} \quad q(\mathbf{u}_{1:K} | \mathbf{u}_0) = \prod_{k=1}^K q(\mathbf{u}_k | \mathbf{u}_0) = \prod_{k=1}^K \mathcal{N}(\mathbf{u}_k | \mathbf{F}(t_k) \mathbf{u}_0, \sigma^2 \mathbf{I}).$$

Taking the negative of the evidence lower bound, we get

$$-\log p_\theta(\mathbf{u}_0) \leq \mathbb{E}_{q(\mathbf{u}_{1:K} | \mathbf{u}_0)} \left[ -\log \frac{p_\theta(\mathbf{u}_{0:K})}{q(\mathbf{u}_{1:K} | \mathbf{u}_0)} \right] \quad (24)$$

$$= \mathbb{E}_{q(\mathbf{u}_{1:K} | \mathbf{u}_0)} \left[ -\log \frac{p(\mathbf{u}_K) \prod_{k=1}^K p_\theta(\mathbf{u}_{k-1} | \mathbf{u}_k)}{\prod_{k=1}^K q(\mathbf{u}_k | \mathbf{u}_0)} \right] \quad (25)$$

$$= \mathbb{E}_{q(\mathbf{u}_{1:K} | \mathbf{u}_0)} \left[ -\log \frac{p_\theta(\mathbf{u}_K)}{q(\mathbf{u}_K | \mathbf{u}_0)} - \log \prod_{k=2}^K \frac{p_\theta(\mathbf{u}_{k-1} | \mathbf{u}_k)}{q(\mathbf{u}_{k-1} | \mathbf{u}_0)} - \log p_\theta(\mathbf{u}_0 | \mathbf{u}_1) \right] \quad (26)$$

$$= \mathbb{E}_{q(\mathbf{u}_{1:K} | \mathbf{u}_0)} \left[ -\log \frac{p_\theta(\mathbf{u}_K)}{q(\mathbf{u}_K | \mathbf{u}_0)} - \sum_{k=2}^K \log \frac{p_\theta(\mathbf{u}_{k-1} | \mathbf{u}_k)}{q(\mathbf{u}_{k-1} | \mathbf{u}_0)} - \log p_\theta(\mathbf{u}_0 | \mathbf{u}_1) \right] \quad (27)$$

$$\begin{aligned} &= \mathbb{E}_{q(\mathbf{u}_{1:K-1} | \mathbf{u}_0)} \int q(\mathbf{u}_K | \mathbf{u}_0) \log \frac{q(\mathbf{u}_K | \mathbf{u}_0)}{p_\theta(\mathbf{u}_K)} d\mathbf{u}_K \\ &\quad + \sum_{k=2}^K \mathbb{E}_{q(\mathbf{u}_{\{1:K\} \setminus \{k-1\}} | \mathbf{u}_0)} \int q(\mathbf{u}_{k-1} | \mathbf{u}_0) \log \frac{q(\mathbf{u}_{k-1} | \mathbf{u}_0)}{p_\theta(\mathbf{u}_{k-1} | \mathbf{u}_k)} d\mathbf{u}_{k-1} \\ &\quad - \mathbb{E}_{q(\mathbf{u}_{1:K} | \mathbf{u}_0)} \log p_\theta(\mathbf{u}_0 | \mathbf{u}_1) \end{aligned} \quad (28)$$

$$\begin{aligned} &= \mathbb{E}_{q(\mathbf{u}_{1:K-1} | \mathbf{u}_0)} \text{D}_{\text{KL}}[q(\mathbf{u}_K | \mathbf{u}_0) \| p(\mathbf{u}_K)] \\ &\quad + \sum_{k=2}^K \mathbb{E}_{q(\mathbf{u}_{\{1:K\} \setminus \{k-1\}} | \mathbf{u}_0)} \text{D}_{\text{KL}}[q(\mathbf{u}_{k-1} | \mathbf{u}_0) \| p(\mathbf{u}_{k-1} | \mathbf{u}_k)] \\ &\quad - \mathbb{E}_{q(\mathbf{u}_{1:K} | \mathbf{u}_0)} \log p_\theta(\mathbf{u}_0 | \mathbf{u}_1) \end{aligned} \quad (29)$$

In the KL terms  $\text{D}_{\text{KL}}[q(\mathbf{u}_{k-1} | \mathbf{u}_0) \| p(\mathbf{u}_{k-1} | \mathbf{u}_k)]$ , the time steps  $k-1$  have already been integrated over and the term is dependent only on  $\mathbf{u}_k$  when  $\mathbf{u}_0$  is constant. The term  $\text{D}_{\text{KL}}[q(\mathbf{u}_K | \mathbf{u}_0) \| p(\mathbf{u}_K)]$  is not dependent on any of the variables  $k$  and  $\log p_\theta(\mathbf{u}_0 | \mathbf{u}_1)$  only on  $\mathbf{u}_1$ . We can proceed in two ways: Either (i) add dummy integrals over the already marginalized over dimensions to get Eq. (7) in the main text, or (ii) marginalize out all redundant expectation values to explicitly get the final loss function. We first look at (i):

$$\begin{aligned} &\mathbb{E}_{q(\mathbf{u}_{1:K-1} | \mathbf{u}_0)} \int q(\mathbf{u}'_K | \mathbf{u}_0) d\mathbf{u}'_K \underbrace{\text{D}_{\text{KL}}[q(\mathbf{u}_K | \mathbf{u}_0) \| p(\mathbf{u}_K)]}_{\text{Not dependent on } \mathbf{u}'_K} \\ &\quad + \sum_{k=2}^K \mathbb{E}_{q(\mathbf{u}_{\{1:K\} \setminus \{k-1\}} | \mathbf{u}_0)} \int q(\mathbf{u}'_{k-1} | \mathbf{u}_0) d\mathbf{u}'_{k-1} \underbrace{\text{D}_{\text{KL}}[q(\mathbf{u}_{k-1} | \mathbf{u}_0) \| p(\mathbf{u}_{k-1} | \mathbf{u}_k)]}_{\text{Not dependent on } \mathbf{u}_{k-1}} \\ &\quad - \mathbb{E}_{q(\mathbf{u}_{1:K} | \mathbf{u}_0)} \log p_\theta(\mathbf{u}_0 | \mathbf{u}_1) \end{aligned} \quad (30)$$

$$\begin{aligned} &= \mathbb{E}_{q(\mathbf{u}_{1:K} | \mathbf{u}_0)} \left[ \underbrace{\text{D}_{\text{KL}}[q(\mathbf{u}_K | \mathbf{u}_0) \| p(\mathbf{u}_K)]}_{L_K} + \sum_{k=2}^K \underbrace{\text{D}_{\text{KL}}[q(\mathbf{u}_{k-1} | \mathbf{u}_0) \| p_\theta(\mathbf{u}_{k-1} | \mathbf{u}_k)]}_{L_{k-1}} \right. \\ &\quad \left. - \underbrace{\log p_\theta(\mathbf{u}_0 | \mathbf{u}_1)}_{L_0} \right], \end{aligned} \quad (31)$$

which is the formula presented in the main text. On path (ii), marginalizing redundant integrals to get the loss function, we get

$$\underbrace{\text{D}_{\text{KL}}[q(\mathbf{u}_K | \mathbf{u}_0) \| p(\mathbf{u}_K)]}_{L_K} + \sum_{k=2}^K \mathbb{E}_{q(\mathbf{u}_k | \mathbf{u}_0)} \underbrace{\text{D}_{\text{KL}}[q(\mathbf{u}_{k-1} | \mathbf{u}_0) \| p_\theta(\mathbf{u}_{k-1} | \mathbf{u}_k)]}_{L_{k-1}} - \mathbb{E}_{q(\mathbf{u}_1 | \mathbf{u}_0)} \underbrace{\log p_\theta(\mathbf{u}_0 | \mathbf{u}_1)}_{L_0}. \quad (32)$$

The first term is constant. As all distributions are defined as Gaussians with diagonal covariance matrices, we get

$$\mathbb{E}_{q(\mathbf{u}_k | \mathbf{u}_0)}[L_{k-1}] = \frac{1}{2} \left( \frac{\sigma^2}{\delta^2} N - N + \frac{1}{\delta^2} \mathbb{E}_{q(\mathbf{u}_k | \mathbf{u}_0)} \left[ \|\mu_\theta(\mathbf{u}_k, k) - F(t_{k-1})\mathbf{u}_0\|_2^2 \right] + 2N \log \frac{\delta}{\sigma} \right), \quad (33)$$

$$\mathbb{E}_{q(\mathbf{u}_1 | \mathbf{u}_0)}[L_0] = \mathbb{E}_{q(\mathbf{u}_1 | \mathbf{u}_0)}[-\log p_\theta(\mathbf{u}_0 | \mathbf{u}_1)] \quad (34)$$

$$= \frac{1}{2\delta^2} \mathbb{E}_{q(\mathbf{u}_1 | \mathbf{u}_0)} \left[ \|\mu_\theta(\mathbf{u}_1, 1) - \mathbf{u}_0\|_2^2 \right] + N \log(\delta\sqrt{2\pi}). \quad (35)$$

Taking a Monte Carlo estimate of the expectations by sampling once from  $\mathbf{u}_k$  or  $\mathbf{u}_1$  and passing it through the neural network  $\mu_\theta$ , we arrive at our final loss function.

### A.3 Variational Upper Bound on $L_K$

In the main text, we noted that  $L_K = D_{\text{KL}}[q(\mathbf{u}_K | \mathbf{u}_0) | p(\mathbf{u}_K)]$  is not trivial to evaluate if we define  $p(\mathbf{u}_K)$  to be a kernel density estimator over the training set, since evaluation of  $p(\mathbf{u}_K)$  is heavy due to the large amount of components. For each spatial location in the integral, we would need to re-evaluate its distance to all blurred training data points, and this is highly inefficient. We can, however, provide a further upper variational upper bound, similarly to [23]:

$$D_{\text{KL}}[q(\mathbf{u}_K | \mathbf{u}_0) | p(\mathbf{u}_K)] = \mathbb{E}_{q(\mathbf{u}_K | \mathbf{u}_0)}[\log q(\mathbf{u}_K | \mathbf{u}_0) - \log p(\mathbf{u}_K)] \quad (36)$$

$$= \mathbb{E}_{q(\mathbf{u}_K | \mathbf{u}_0)}[\log q(\mathbf{u}_K | \mathbf{u}_0) - \log \frac{1}{N_T} \sum_{i=1}^{N_T} \mathcal{N}(\mathbf{u}_K | \mathbf{u}_K^i, \sigma^2)], \quad (37)$$

where  $N_T$  is the training set size and  $\mathbf{u}_K^i$  is an example from the training set. The first term is simply the negative entropy of a Gaussian. For the second term, introduce variational parameters  $\phi_i > 0$  such that  $\sum_i \phi_i = 1$ :

$$-\mathbb{E}_{q(\mathbf{u}_K | \mathbf{u}_0)}[\log \frac{1}{N} \sum_{i=1}^{N_T} \mathcal{N}(\mathbf{u}_K | \mathbf{u}_K^i, \delta^2)] = -\mathbb{E}_{q(\mathbf{u}_K | \mathbf{u}_0)} \left[ \log \frac{1}{N} \sum_{i=1}^{N_T} \phi_i \frac{\mathcal{N}(\mathbf{u}_K | \mathbf{u}_K^i, \delta^2)}{\phi_i} \right] \quad (38)$$

$$\leq -\mathbb{E}_{q(\mathbf{u}_K | \mathbf{u}_0)} \sum_i \phi_i \log \left[ \frac{\mathcal{N}(\mathbf{u}_K | \mathbf{u}_K^i, \delta^2)}{N_T \phi_i} \right] \quad (39)$$

$$= -\sum_i \phi_i [\mathbb{E}_{q(\mathbf{u}_K | \mathbf{u}_0)}[\log \mathcal{N}(\mathbf{u}_K | \mathbf{u}_K^i, \delta^2)] - \log N_T \phi_i] \quad (40)$$

$$= -\sum_i \phi_i [-H(q(\mathbf{u}_K | \mathbf{u}_0), \mathcal{N}(\mathbf{u}_K | \mathbf{u}_K^i, \delta^2)) - \log N_T - \log \phi_i]. \quad (41)$$

Note that the cross-entropy between Gaussians has an analytical formula that can be precomputed for all training set - test set sample pairs. Minimizing the upper bound w.r.t.  $\phi_i$ , we get

$$\phi_i = \frac{e^{-D_{\text{KL}}(q(\mathbf{u}_K | \mathbf{u}_0) | \mathcal{N}(\mathbf{u}_K | \mathbf{u}_K^i, \delta^2))}}{\sum_j e^{-D_{\text{KL}}(q(\mathbf{u}_K | \mathbf{u}_0) | \mathcal{N}(\mathbf{u}_K | \mathbf{u}_K^j, \delta^2))}}. \quad (42)$$

Now, we just need to evaluate the KL divergences between data points in the training set and the test set, and then we can use those to calculate the upper bound efficiently, without need to integrate over and evaluate  $p(\mathbf{u}_K)$  multiple times in a very high-dimensional space. Calculation of the KL divergences amounts to calculating the distances of blurry data points in the training and test sets.

While the calculations are straightforward to implement in practice, one needs to be a bit careful when doing the computations numerically. In particular, we can use the log-sum-exp trick to estimate  $\log \phi_i$  in a numerically stable way, and  $\phi_i$  is obtained from the  $\log \phi_i$  values.

## B Experiment Details

### B.1 Neural Network Architecture and Hyperparameters

Similarly to many recent works on diffusion models [24, 75, 55, 18], we use a U-Net architecture for estimating the transitions, and in particular parametrize  $\mu_\theta(\mathbf{u}_k, k) = \mathbf{u}_k + f_\theta(\mathbf{u}_k, k)$ , where  $f_\theta(\mathbf{u}_k, k)$



Table 1: Neural network hyperparameters.

Data	Resolution	Layer multipliers	Base channels	Learning rate	Self-attention resolutions	EMA	Batch size	# Res-blocks
MNIST	28×28	(1,2,2)	128	1e-4	7×7	0.999	128	4
CIFAR-10	32×32	(1, 2, 2, 2)	128	2e-4	8×8, 4×4	0.999	128	4
FFHQ	256×256	(1, 2, 3, 4, 5)	128	2e-5	64×64, 32×32, 16×16	0.9999	32	2
FFHQ	128×128	(1, 2, 3, 4, 5)	128	2e-5	32×32, 16×16, 8×8	0.999	32	2
AFHQ	256×256	(1, 2, 3, 4, 5)	128	2e-5	64×64, 32×32, 16×16	0.9999	32	2
AFHQ	64×64	(1, 2, 3, 4)	128	1e-4	16×16, 8×8	0.999	128	2
LSUN CHURCHES	128×128	(1, 2, 3, 4, 5)	128	2e-5	32×32, 16×16, 8×8	0.999	32	2

corresponds to the U-Net, as explained in the main text. Following [18], we use self-attention layers at multiple low-resolution feature maps. Otherwise, the architecture follows the one in [24], and we don’t, *e.g.*, use multiple attention heads or adaptive group normalization [18]. We use two residual blocks per resolution layer in other models than the MNIST and CIFAR-10 models, where we use 4. We use 128 base channels, GroupNorm layers in the residual blocks and a dropout rate of 0.1, applied in each residual block. The downsampling steps in the U-Net were done with average pooling and upsampling steps with nearest-neighbour interpolation. The timestep information is included using a sinusoidal embedding that is added to the feature maps in each residual block. Table 1 lists the values of other hyperparameters that we used on different data sets. They are mostly based on the recent work with diffusion models [24, 55, 18], and haven’t been optimized over. For the lower resolution data sets, we used a higher learning rate of 1e-4 or 2e-4, and a lower learning rate of 2e-5 for the higher resolutions for added stability, although we didn’t sweep over these values. An EMA rate of 0.9999 was also used instead of 0.999 for  $256 \times 256$  images, instead of the 0.999 that was used for other data sets. We used the Adam optimizer with default hyperparameters  $\beta_1 = 0.9$ ,  $\beta_2 = 0.999$  and  $\varepsilon = 10^{-8}$ . We also use gradient norm clipping with rate 1.0 and learning rate warm up by linearly interpolating it from 0 to the desired learning during the first 5000 steps. We don’t add noise on the final step of the generative process, as that can’t increase the output quality. Other details are included in the code release.

We used random horizontal flips on AFHQ, and no data augmentation on the other data sets.

## B.2 Training Time and Computational Resources

We use NVIDIA A100 GPUs for the experiments, with two GPUs for  $256 \times 256$  resolution models and one GPU for all others. We use the Pytorch automatic mixed precision functionality for a higher per-GPU batch size. On CIFAR-10, we trained for 400 000 iterations, taking 7 hours per 100 000 steps. On the  $256 \times 256$  images, 100 000 iterations takes about 40 hours, and we used 800 000 iterations on FFHQ and 400 000 iterations on AFHQ. On LSUN-Churches, 100 000 training steps takes 11 hours, and training was continued for one million iterations. On the smaller  $64 \times 64$  AFHQ data set, we trained for 100 000 iterations, taking a total of 14 hours.

## B.3 FID Score Calculation

To calculate FID-scores, we used clean-fid [56], where the generated images and reference images are scaled to  $299 \times 299$  resolution with bicubic interpolation before passing them to the InceptionV3 network. We used 50000 samples to calculate the scores for all other data sets than the  $256 \times 256$  sets, where we used 10000 samples. Using a lower amount of samples results in the values being slightly overestimated, which is not too much of an issue since the FID scores are not very close to state-of-the-art values. We used the training set to calculate the reference statistics on LSUN-CHURCHES and CIFAR-10, and the entire data sets for FFHQ and AFHQ.

## B.4 Hyperparameters Related to the New Generative Process

The different hyperparameters related to the new generative process are listed in Table 2. Early on during experimentation, we noticed that  $\sigma = 0.01$  for the training noise seems to work well, and use that for all experiments unless mentioned otherwise. We haven’t done an extensive study on the optimal value. The number of iteration steps  $K$  was set to 200 for most experiments, except for

Table 2: Hyperparameters related to the generative process.

Data	Resolution	K	$\sigma_{B,\max}$	$\sigma$	$\delta$
MNIST	28×28	100	20	0.01	0.0125
CIFAR-10	32×32	200	24	0.01	0.01325
FFHQ	256×256	200	128	0.01	0.0125
FFHQ	128×128	200	128	0.01	0.0125
AFHQ	256×256	200	128	0.01	0.01275
AFHQ	64×64	200	32	0.01	0.0125
LSUN CHURCHES	128×128	400	64	0.01	0.0125

the LSUN CHURCHES data set, where we noted that  $K = 400$  increased sample quality slightly. Otherwise, in contrast to findings on diffusion models [24], we found in early experimentation that increasing the number of steps well above 200 didn’t seem to result in trivial improvements in sample quality. On MNIST, we used 100 steps. Although a  $\delta$  of 0.0125 =  $1.25 \times \sigma$  seemed to work well as a default value on all data sets, we tuned it to 0.01325 on CIFAR-10 by sweeping over the FIDs obtained with different values (results visualized in App. C.1). On AFHQ 256 × 256, we set it to 0.01275 because visual inspection showed slightly improved results. The maximal effective blurring length-scale,  $\sigma_{B,\max}$ , was set to half the size of the images in most experiments, although on MNIST and CIFAR-10 we used slightly higher values. We noticed during early experimentation that moving  $\sigma_{B,\max}$  from the entire image width to half the width resulted in better image quality, although the information content present in the half-blurred image is intuitively not much different from the information content in the fully averaged out image. We also study how  $\sigma_{B,\max}$  affects the value of the prior overlap term  $D_{\text{KL}}[q(\mathbf{u}_K | \mathbf{u}_0) || p(\mathbf{u}_K)]$  in App. C.2 on CIFAR-10, providing justification to not having  $\sigma_{B,\max} = \text{entire image width}$ .

### B.5 Schedule on $t_k$

In all experiments, we used a logarithmic spacing for the time steps  $t_k$ , where  $t_K = \sigma_{B,\max}^2/2$  and  $t_1 = \sigma_{B,\min}^2/2 = 0.5^2/2$ , corresponding to sub-pixel-size blurring. Effective averaging sizes  $\sigma_{B,\min}$  on other levels were then interpolated with  $\sigma_{B,k} = \exp(\log \sigma_{B,\min} \frac{K-k}{K-1} + \log \sigma_{B,\max} \frac{k-1}{K-1})$  for an even spacing on a logarithmic axis. We can view the  $\sigma_B$  schedule in two ways: First, it corresponds to a constant rate of resolution decrease, in the sense that  $\frac{\sigma_{B,k+1}}{\sigma_{B,k}}$  is constant. Second, we can explicitly visualize the rate of effective dimensionality decrease by looking at the frequency components in the discrete cosine transform as we increase  $\sigma_B = \sqrt{2t}$ . When they pass well below the  $\sigma^2 = 0.01^2$  line, the frequency components become indistinguishable from noise in the forward process  $q(\mathbf{u}_k | \mathbf{u}_0) = \mathcal{N}(\mathbf{u}_k | \mathbf{F}(t_k) \mathbf{u}_0, \sigma^2 \mathbf{I})$ . This is done in Fig. 9, where we see that with a logarithmic spacing on  $\sigma_B$  (and  $t_k$ ), the amount of remaining frequencies decreases at an approximately constant rate, although slows down somewhat towards the end.

### B.6 Calculation of 1D Power Spectral Densities

The 2D DCT has a 2D output, and to get the 1D plots of PSD with respect to frequency, *e.g.*, Fig. 4, we take the average PSDs over equal-frequency contours. This is visualized in Fig. 10 for an example image.

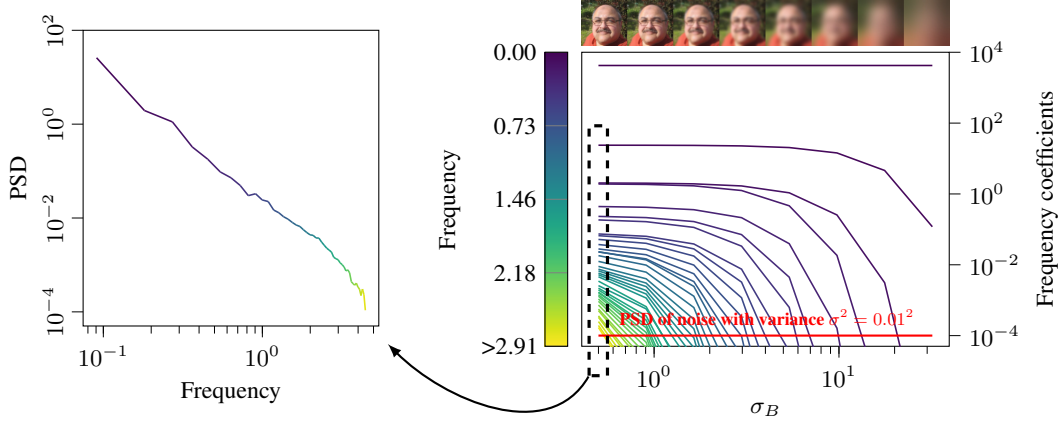


Figure 9: Squared frequency components in the discrete cosine transform of the example image as a function of the effective blurring width  $\sigma_B$ . As the heat equation progresses, the more frequency components become indistinguishable from the training noise  $\sigma$ . Each vertical slice on the plot on the right corresponds to a 1D PSD, such as the one on the left. The values are averages over equal-frequency contours in the full 2D DCT.

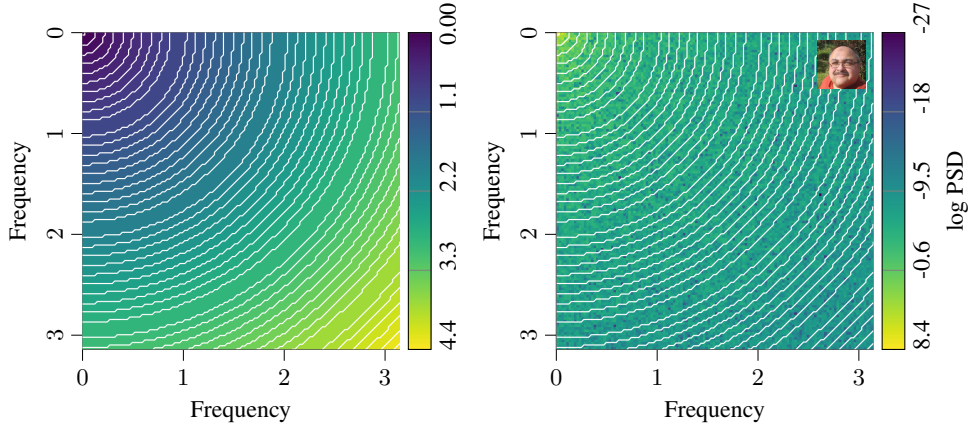


Figure 10: Left: The partitioning of frequencies in the 2D Discrete Cosine Transform. Right: The PSD from the discrete cosine transform of an example image, with the partitions. The one-dimensional power spectral densities, *e.g.*, in Fig. 4, are obtained by averaging the PSDs along the equal-frequency contours.

## C Additional experiments

### C.1 The optimal $\delta$ with respect to marginal log-likelihood vs. FID

We point out that the optimal NLL scores with respect to  $\delta$  don't correspond to the optimal  $\delta$  for FID values. We plot the negative per-sample ELBO and FID values in Fig. 11, where we see that the lowest NLL is achieved close to  $\sigma = 0.01$ , whereas the lowest FID score is got somewhere near 0.01325, which is our chosen value for  $\delta$ , listed in Table 2. To get an intuition to the result, consider the  $L_k$  terms in the loss ELBO:

$$\mathbb{E}_q[L_{k-1}] = \mathbb{E}_q[\text{D}_{\text{KL}}[q(\mathbf{u}_{k-1} | \mathbf{u}_0) \| p_\theta(\mathbf{u}_{k-1} | \mathbf{u}_k)]] \quad (43)$$

$$= \frac{1}{2} \left( \frac{\sigma^2}{\delta^2} N - N + \frac{1}{\delta^2} \mathbb{E}_{q(\mathbf{u}_k | \mathbf{u}_0)} \left[ \|\mu_\theta(\mathbf{u}_k, k) - \mathbf{F}(t_{k-1}) \mathbf{u}_0\|_2^2 \right] + 2N \log \frac{\delta}{\sigma} \right). \quad (44)$$

Without the MSE term in the KL divergences  $L_k$ , the optimal values for  $\delta$  is always  $\sigma$ , as can be seen by straightforward differentiation of the  $\frac{\sigma^2}{\delta^2} N$  and  $2N \log \frac{\delta}{\sigma}$  terms. The inclusion of the MSE term nudges the optimal  $\delta$  to a higher value, but if the MSE loss is not very high, then it doesn't get

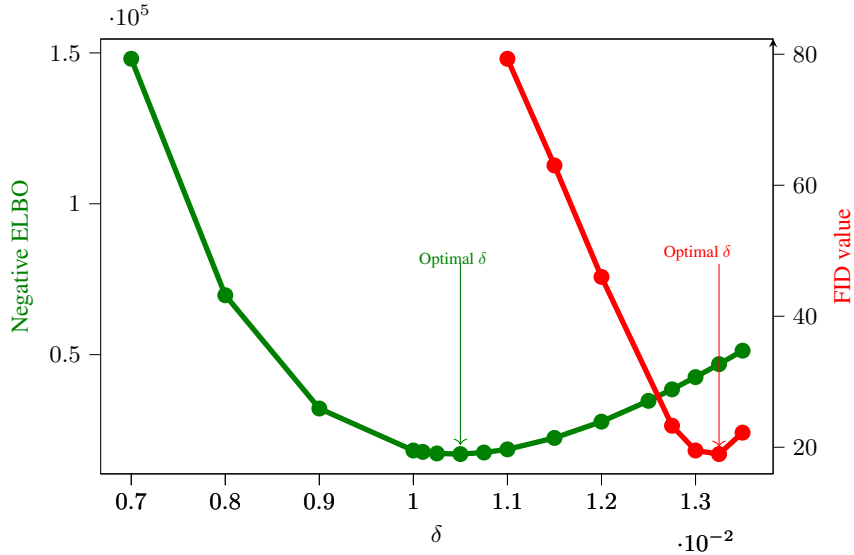


Figure 11: The per-sample negative ELBO and FID values as a function of  $\delta$  on our CIFAR-10 model.

nudged by a lot. Changing the value of  $\sigma$  would likely change the picture, but it appears that our model is in a regime where  $\frac{\sigma^2}{\delta^2} N$  and  $2N \log \frac{\delta}{\sigma}$  dominate the NLL scores. To improve our model as a marginal log-likelihood maximizer, the interplay of these terms could be studied further to get to a hyperparameter regime where the optimal FID values and NLL values are obtained simultaneously.

## C.2 Evaluation of the Prior in Terms of Overlap with the Test Set

Overlap between the blurred out train and test sets, measured by  $L_K$ , can be used as a prerequisite measure of how we can expect the model to generalize beyond the train set, since we use the training data to draw samples from the prior  $p(\mathbf{u}_K)$ . If  $\sigma_{B,\max} \approx 0$ , then there is almost no overlap at all and the generative process will just be a memorization of the train set. On the other hand, if the data set is fully averaged out at the end of the forward process, then we expect that using samples from the blurry train set as the prior to have a high overlap with the blurry test set since both distributions are essentially low-dimensional. To showcase the situation with our CIFAR-10 model, we plot the average  $L_K$  values on the test set with respect to  $\sigma_{B,\max}$ . We see that it decreases as the maximal effective length-scale is increased, and doesn't change much moving from 24 to 32. Thus, there doesn't seem to be reason to believe that increasing  $\sigma_{B,\max}$  would result in much better generalization.

## C.3 The Importance of Non-zero Training Noise $\sigma$

As noted in the main paper, the model is almost as simple as possible. Here we show that one complication, the inclusion of sampling noise  $\sigma$  is necessary for the model to work. As an example, Fig. 13a shows samples from a model trained on MNIST with  $\sigma = 0$ . The model completely fails to work, resulting in random patterns. Figure 13b shows the generative process and visualizes neural network input gradients during the process, both for zero sampling noise,  $\delta = 0$ , and with a non-zero amount of sampling noise. The trajectory starts from the flat image, but quickly blows up to a random pattern, especially with noise added during sampling. Note that the input gradients are similar to the ones seen in Fig. 8 for our model, but the signs are the opposite. Intuitively, it appears that the model has learned a generic sharpening filter where the response of the output grows as the input image gets less blurry. Without the sampling noise  $\sigma$ , the model learns to literally take steps along the ill-posed inverse heat equation, but with a non-zero  $\sigma$ , the model becomes more robust, and takes the training data distribution into account.

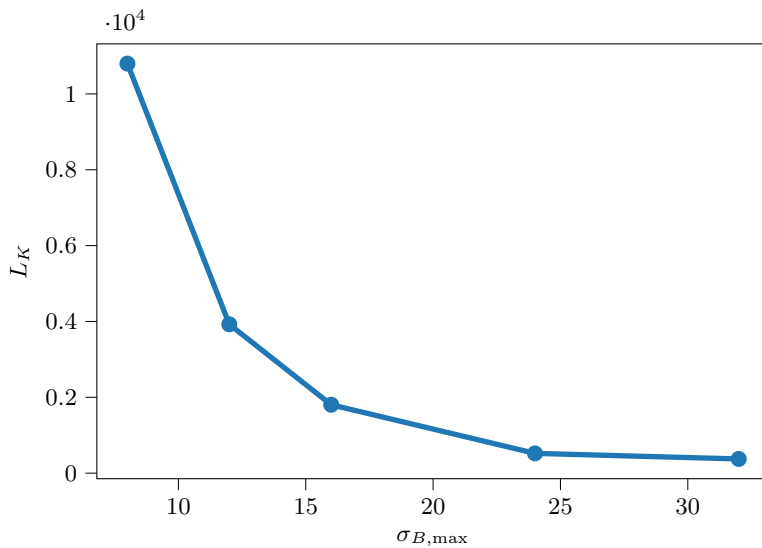


Figure 12: Average values of the  $L_K$  term on the CIFAR-10 test set, with respect to the maximum effective blurring width  $\sigma_{B,\max}$ .  $L_K$  effectively measures how large is the overlap between the averaged out test distribution and the averaged out train distribution, which is used as the prior distribution in the model.

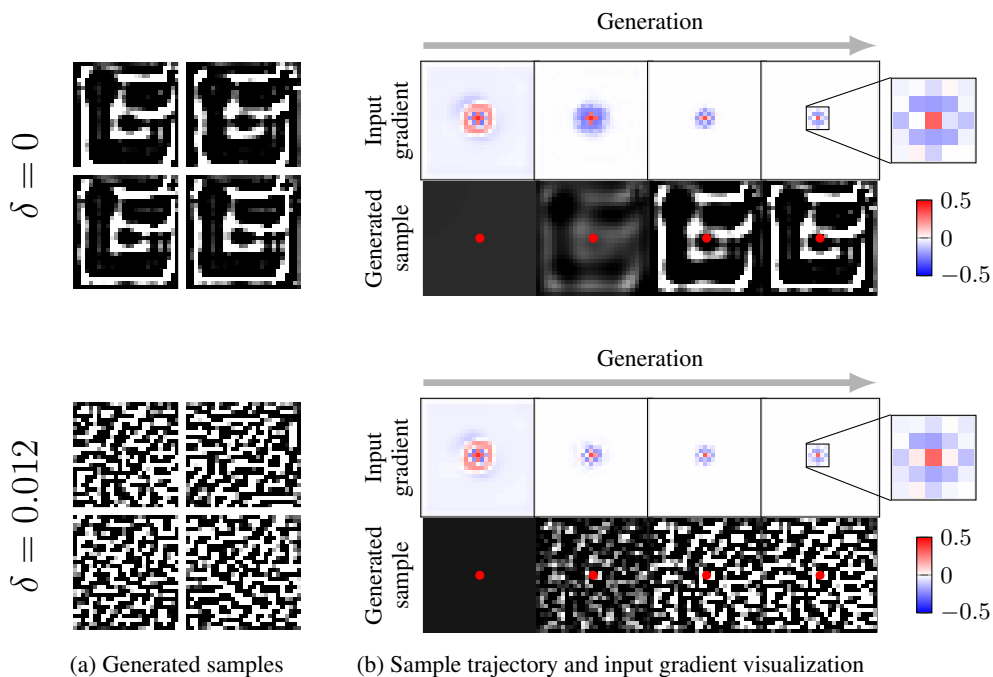


Figure 13: Failure of the model when  $\sigma = 0$ . (a) Generated samples from a model trained on MNIST with the training noise parameter  $\sigma = 0$ . (b) Generative trajectory and neural network input gradients for the pixel highlighted in red. Note that the input gradients resemble the ones seen in Fig. 8 for our model, but the signs are exactly the opposites. The colours are scaled to a symlog scale with a linear cutoff at 0.002.



## D Sample visualizations

In this section, we start by showcasing uncurated samples on the different data sets we trained our models on in App. D.1. We then showcase the finding that interpolating the noise and starting image results in smooth interpolations in the output image in our model in App. D.2. In App. D.3 we provide further examples of the result where the overall colour and other features of images can become disentangled in our model. Finally, in App. D.4, we plot example Euclidean nearest neighbours of samples from our model, showcasing that the generated samples are not just approximations of training set images.

In the interpolation results, the prior states  $\mathbf{u}_K$  are interpolated linearly. The noises are interpolated with a spherical interpolation  $\sin(\phi)\nu_1 + \cos(\pi/2 - \phi)\nu_2$ , where  $\nu_1$  and  $\nu_2$  are the noise vectors and  $\phi \in [0, \frac{\pi}{2}]$ . The reason is that when we sample two random high-dimensional standard Gaussian noise vectors, they are, with high probability, approximately orthogonal to each other, with approximately equal magnitudes. In a linear interpolation between two orthogonal, equal magnitude vectors, the magnitude of the interpolated vector will decrease half-way. In Fig. 6 we saw that decreasing the magnitude of the sampling noise has a large effect on the results, and really we want the magnitude to remain constant during interpolation. This is achieved with spherical interpolation, where the vector is moved along the surface of a hypersphere between the two orthogonal vectors  $\nu_1$  and  $\nu_2$ .

### D.1 Additional Samples



Figure 14: Uncurated samples on MNIST.

Initial state ←————— Generated samples —————→



Figure 15: Uncurated samples on MNIST, with shared initial states  $\mathbf{u}_K$ .

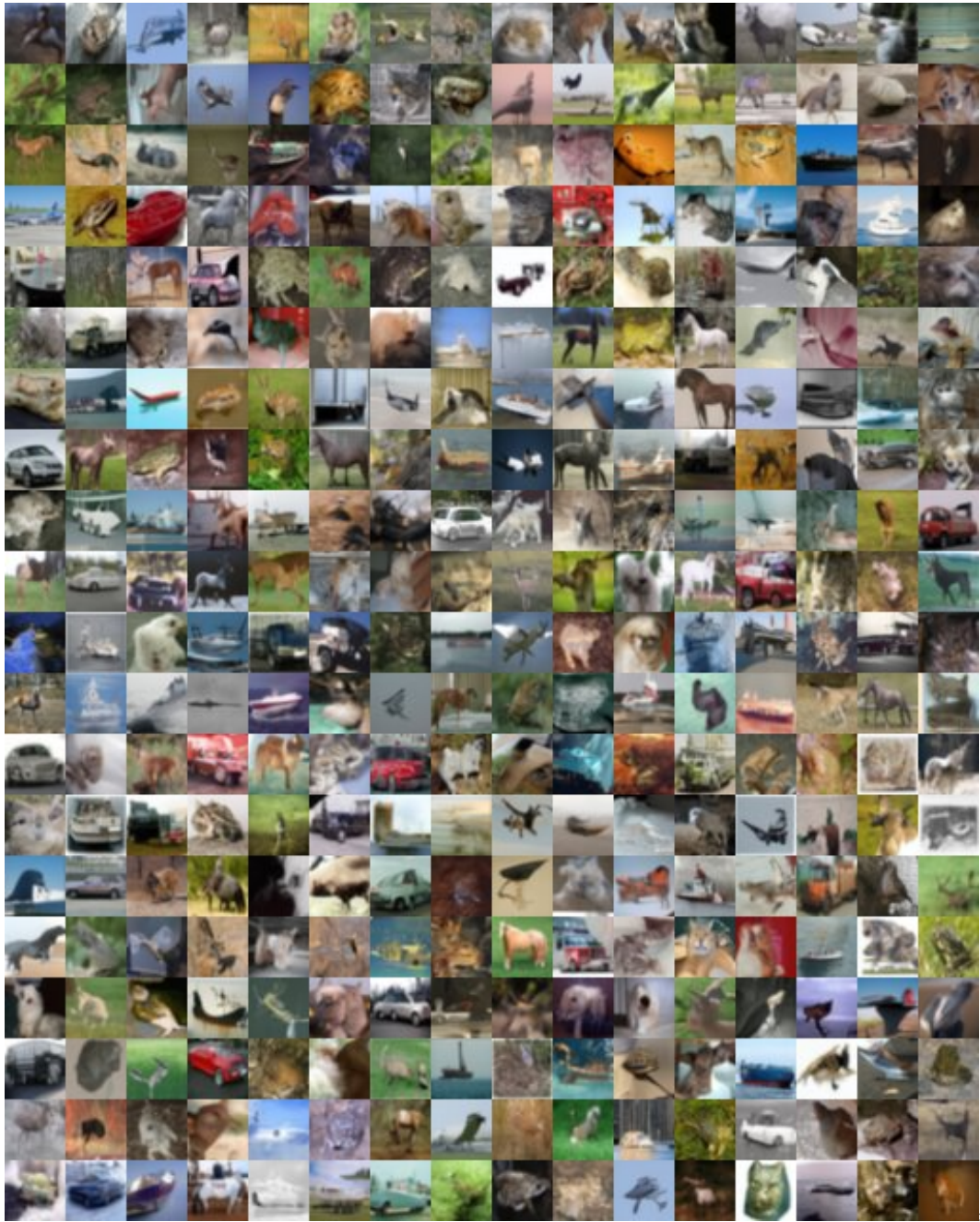


Figure 16: Uncurated samples on CIFAR-10. FID 18.96.

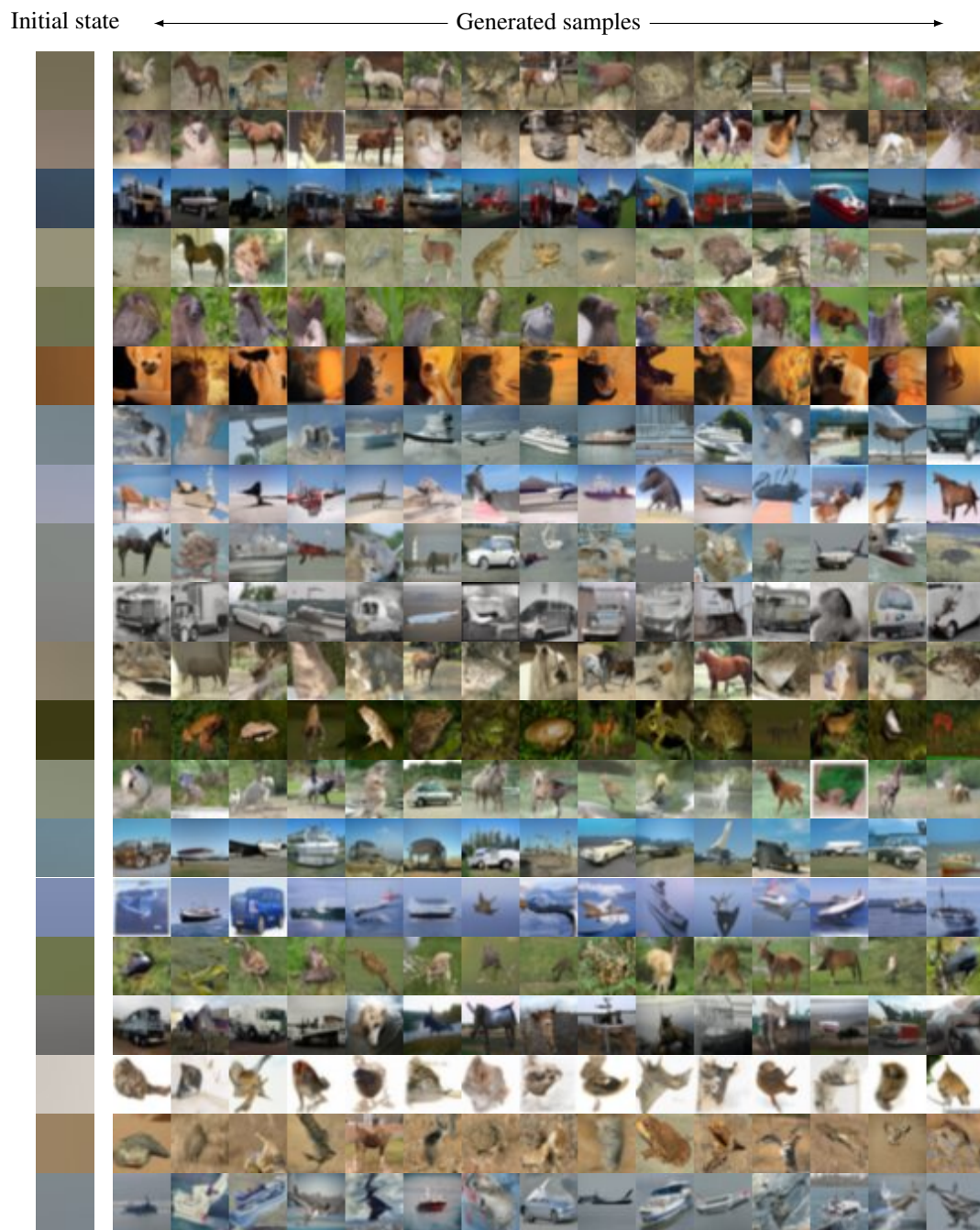


Figure 17: Uncurated samples on CIFAR-10, with shared initial states  $\mathbf{u}_K$ .











Figure 20: Uncurated samples on AFHQ  $64 \times 64$ . FID 14.78.

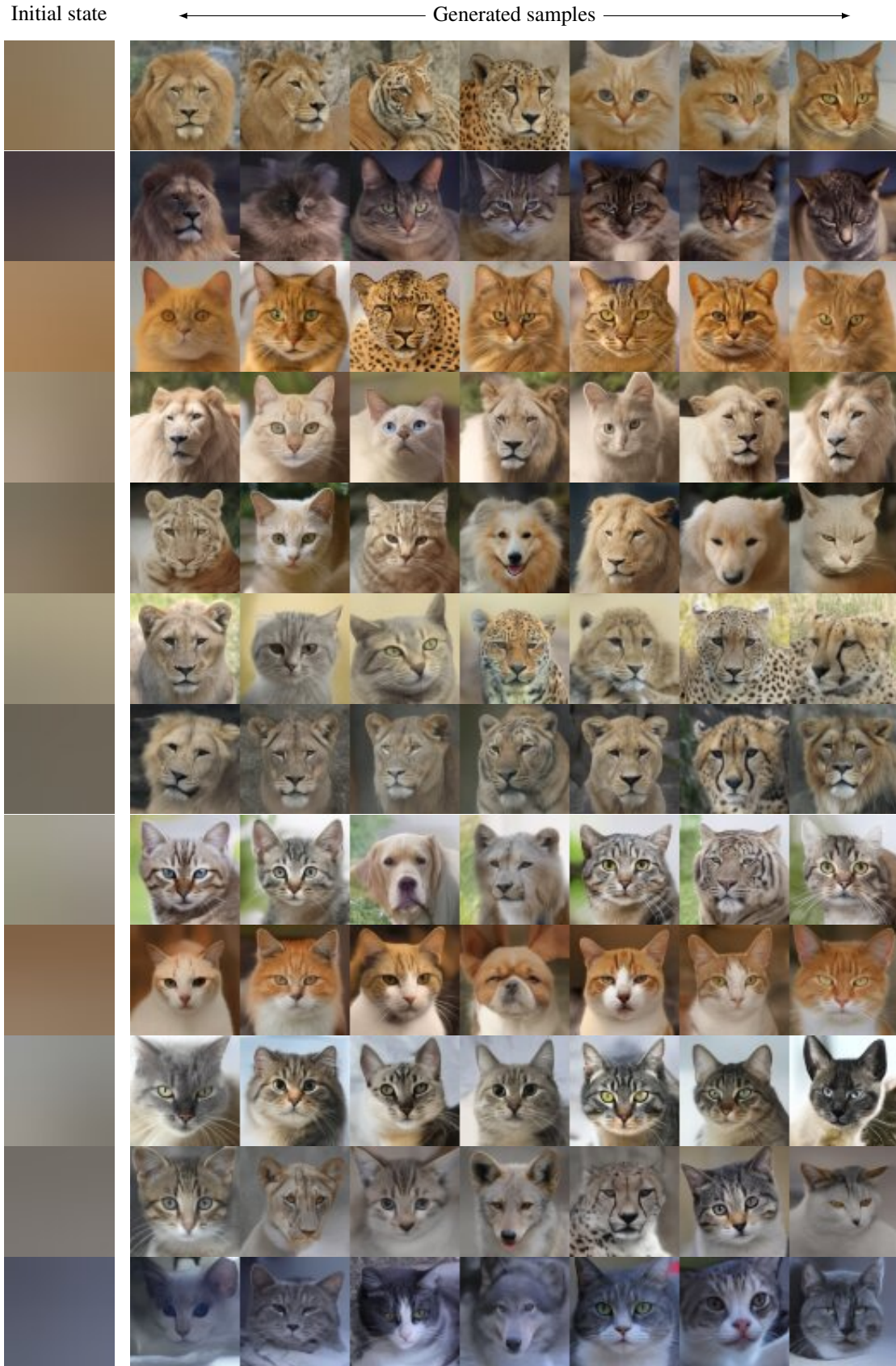


Figure 21: Uncurated samples on AFHQ  $64 \times 64$ , with shared initial states  $\mathbf{u}_K$ .





Figure 22: Uncurated samples on FFHQ  $256 \times 256$ . FID 64.91.



Figure 23: Uncurated samples on FFHQ  $256 \times 256$ , with shared initial states  $\mathbf{u}_K$ .





Figure 24: Uncurated samples on AFHQ  $256 \times 256$ . FID 43.49.

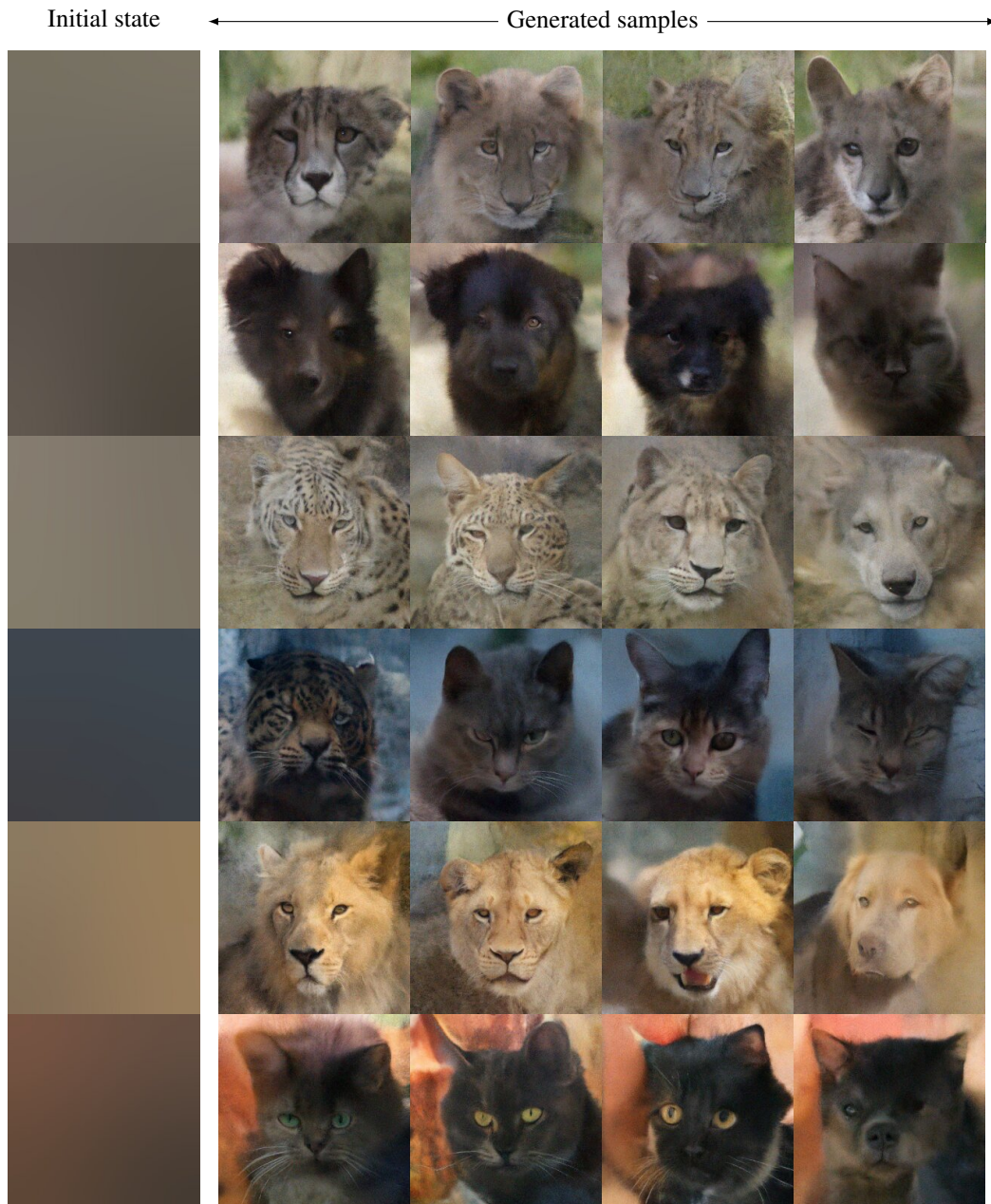


Figure 25: Uncurated samples on AFHQ  $256 \times 256$ , with shared initial states  $\mathbf{u}_K$ .



## D.2 Interpolations

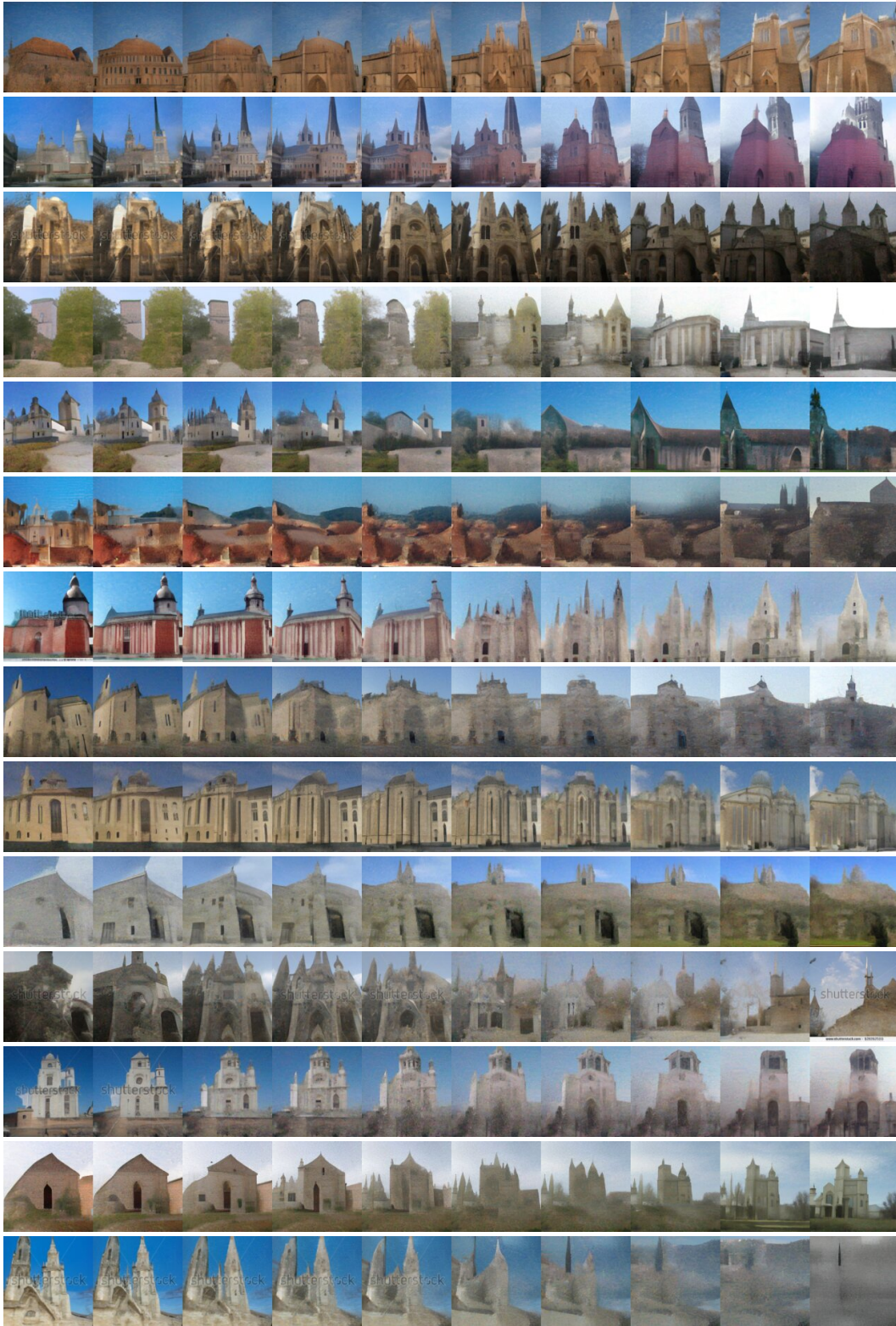


Figure 26: Interpolations between two random images on LSUN-CHURCHES  $128 \times 128$ .



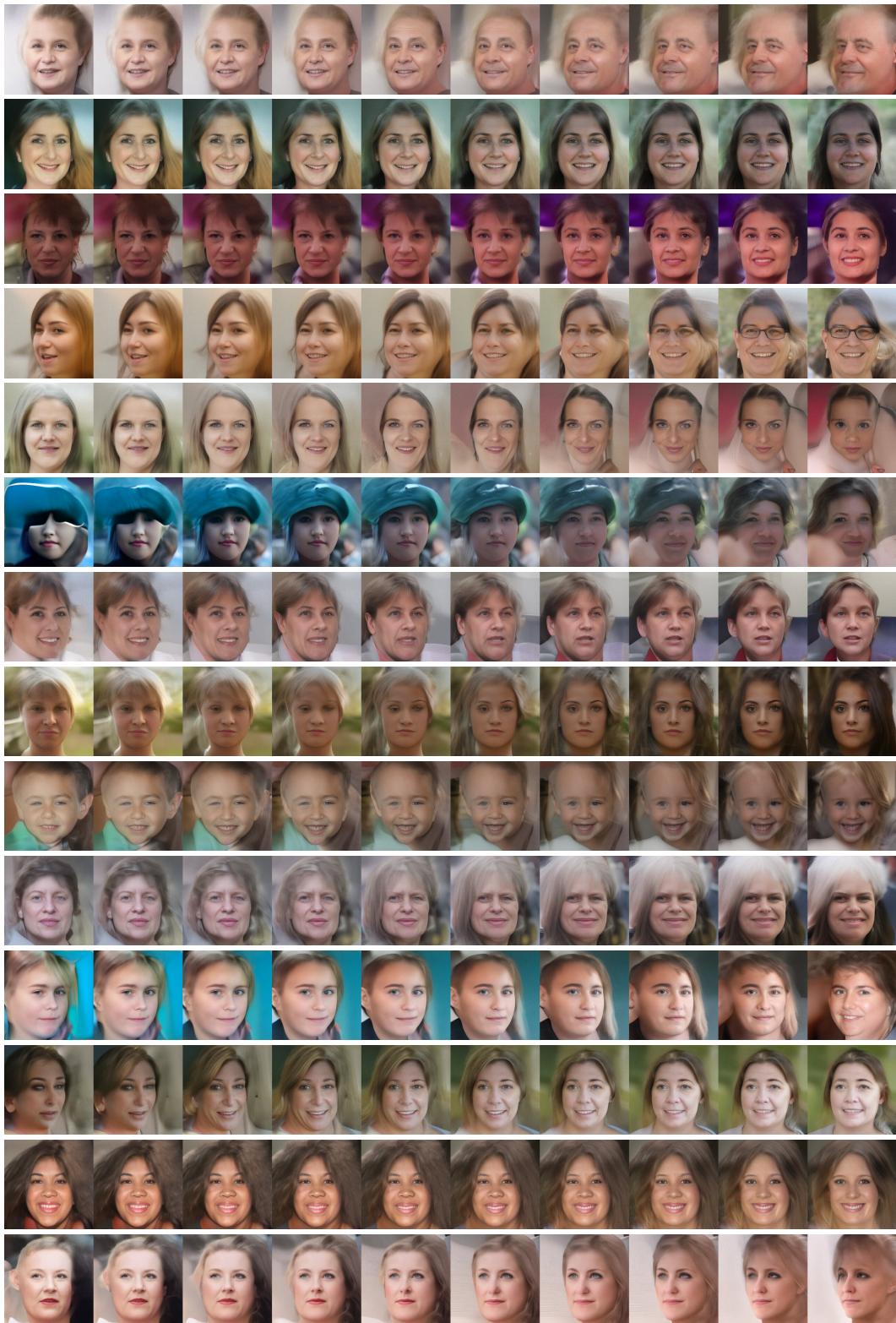


Figure 27: Interpolations between two random images on FFHQ  $256 \times 256$ .





Figure 28: Interpolations between two random images on AFHQ  $64 \times 64$ .

### D.3 Disentanglement of colour and shape by fixing the sampling noise

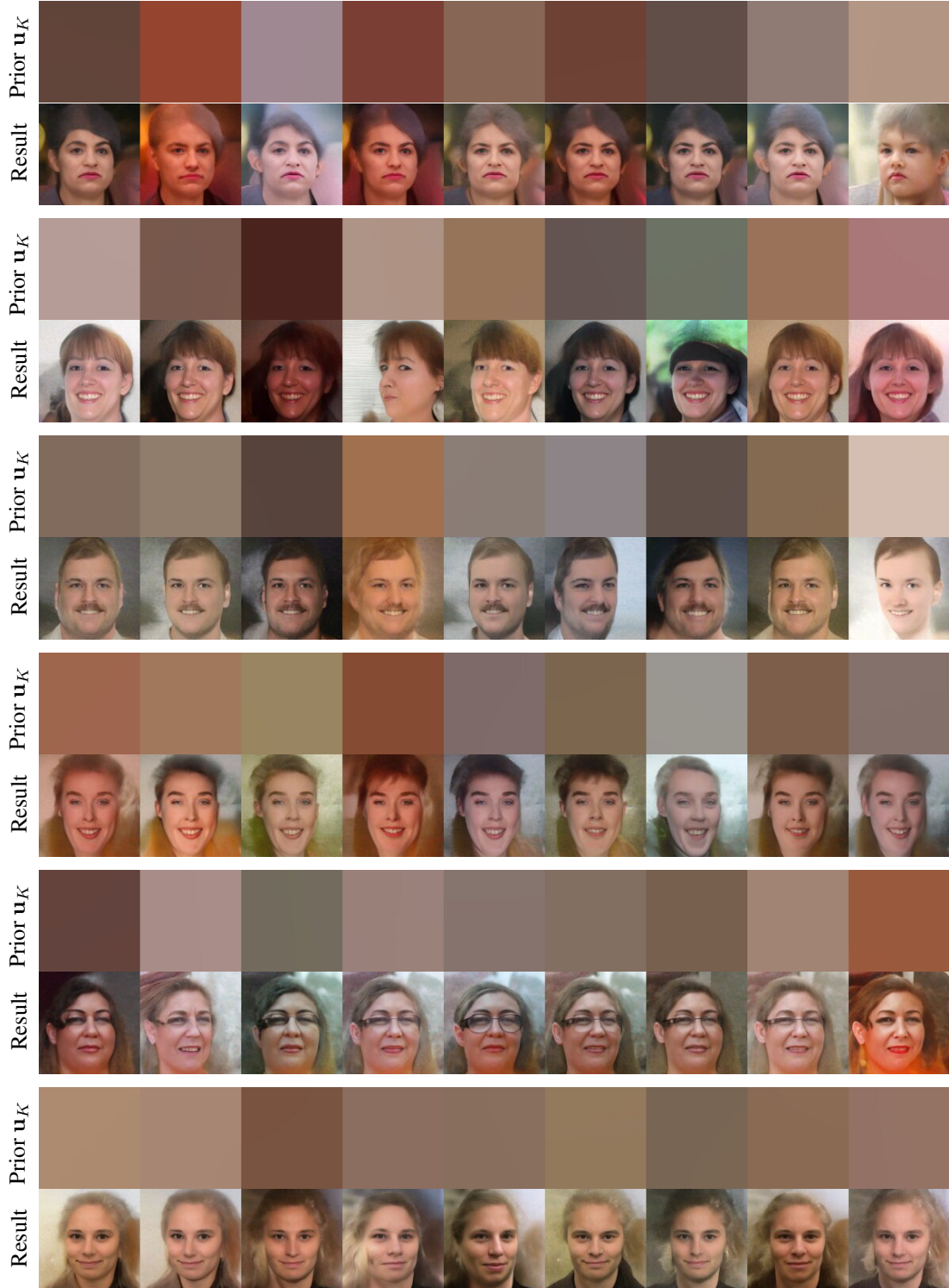


Figure 29: Disentanglement of colour and shape on FFHQ  $128 \times 128$ , where  $\sigma_{B,\max} = 128$ . The noise steps added during the process are fixed, and only the initial state  $p(\mathbf{u}_K)$  is changed, resulting in the model carving out images with very similar characteristics, but with different average colours. The sample quality is somewhat lower on this model than the regular FFHQ model, but it illustrates the effect.



#### D.4 Nearest neighbors on sampled images



Figure 30: Samples on FFHQ vs. their Euclidean nearest neighbors on the training data.

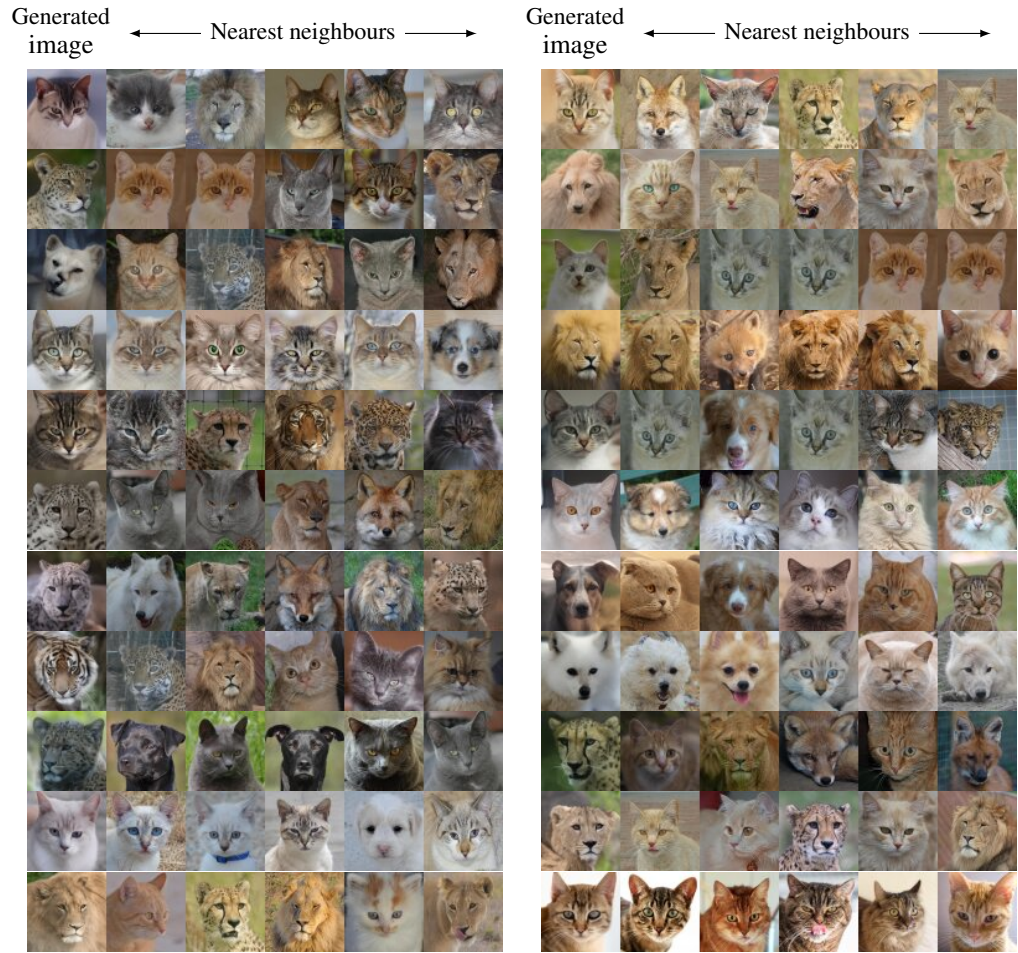


Figure 31: Samples on AFHQ  $64 \times 64$  vs. their Euclidean nearest neighbors on the training data.





Figure 32: Samples on LSUN-CHURCHES  $128 \times 128$  vs. their Euclidean nearest neighbors on the training data.